The Thesis Committee for Matthew Scott Smith

certifies that this is the approved version of the following thesis:

Utilization of Simulated GRACE Inter-Satellite Range-Accelerations to Estimate Earth's Gravity Field

APPROVED BY

SUPERVISING COMMITTEE:

Srinivas Bettadpur, Supervisor

Himanshu Save

Utilization of Simulated GRACE Inter-Satellite Range-Accelerations to Estimate Earth's Gravity Field

by

Matthew Scott Smith

THESIS

Presented to the Faculty of the Graduate School of

The University of Texas at Austin

in Partial Fulfillment

of the Requirements

for the Degree of

MASTER OF SCIENCE IN ENGINEERING

THE UNIVERSITY OF TEXAS AT AUSTIN

December 2018

Acknowledgments

I'd like to express my heartfelt gratitude to my advisor, Dr. Srinivas Bettadpur, who took a chance on a non-traditional student and allowed me the opportunity to make a dream finally come true. I will be forever in his debt. It was an honor and a privilege to be under his guidance, and observe his wisdom and expertise first-hand at the Center for Space Research. I'd also like to thank Dr. Himanshu Save for serving as my second reader, as well as allowing me open door access to his wealth of knowledge on all things GRACE. Additionally, I'd like to commend all the faculty in the orbits area of the Aerospace Department at the University of Texas at Austin for collectively shaping and maintaining an exceptional graduate program. Being under their tutelage prepared me remarkably well for my first position out of school. I am proud to have attended there. A special thank you goes to Dr. Ryan Russell, who was pivotal in helping me clarify and achieve my career goals.

I'd like to make special mention of my partner Kelsey, and all of my Austin family. I cherish all of our shared times together, and all of their unwavering support and love kept me invigorated while on my journey. I am fortunate to have them in my life.

Matthew Scott Smith

Utilization of Simulated GRACE Inter-Satellite Range-Accelerations to Estimate Earth's Gravity Field

Matthew Scott Smith, MSE
The University of Texas at Austin, 2018

Supervisor: Srinivas Bettadpur

The Gravity Recovery and Climate Experiment (GRACE) provides high-precision K-band Ranging (KBR) data which has been instrumental in improving our understanding of the monthly mass redistribution within the Earth system, and consequently its static and time-varying gravity fields. In practice, estimation of the Earth's gravity field with data from GRACE-like missions is typically done via the range-rate pseudo-observations. This approach is widely used and produces high-quality solutions, however there does exist a well-known North-South striping error in the resulting gravity field. It is thought there may be a potential benefit from utilizing instead the range-acceleration pseudo-observations, which should be sensitive to more spatially-localized mass variations in the signal, thereby reducing the N-S errors in the gravity field and facilitating more precise estimation to higher degrees.

Most solutions obtained from range-accelerations to date have been unusable at worst and lesser in quality at best when compared to range-rate derived gravity field solutions. Current understanding is that this is due to the time-differentiation of the KBR signal required to obtain the range-acceleration measurements. The differentiation process acts as a high-pass filter, degrading the signal-to-noise ratio (SNR) at high frequencies, and thus the quality of the solution. The purpose of this work, which explores variational methods solely, is to discover what conditions, if any, make it possible to generate feasible solutions via range-accelerations, and to compare them to one obtained via range-rate. A 180x180 range-rate based gravity field solution produced from simulated August 2008 data was used as a baseline for these comparisons. It is demonstrated that adjusting the parameters of the currently-used filter for obtaining the range-accelerations provides some improvement in the resulting solutions. Conversely, attempts with an alternative approach to filtering the range measurements yielded no benefit over the current method, and only served to degrade the solutions further. However, through an application of filtering the range residuals instead, this research suggests that the culprit is not solely the noise induced by differentiation, but the inclusion of other noisy measurements necessary for the computation of the range-acceleration measurement equation. Through this new method, it is shown that not only are range-accelerations viable for estimating the gravity field, but they can produce solutions more accurate at higher degrees than their range-rate counterparts. While these results are encouraging for processing the range-accelerations, the same technique can be applied to range-rate based solutions, which produces similar improvements and again establishes that quantity as the most suitable for estimating the gravity field, for now.

Table of Contents

List of Tables

List of Figures

Chapter 1

Introduction

The Gravity Recovery and Climate Experiment (GRACE), launched in 2002, was a joint initiative between the National Aeronautics and Space Administration (NASA) and Deutsches Zentrum für Luft-und Raumfahrt (DLR). The mission was a co-investigation between the Center for Space Research (CSR) in Texas, and GeoForschungsZentrum (GFZ) in Germany. The project was managed by NASA's Jet Propulsion Laboratory (JPL), with ground operations taking place at the German Space Operations Center (GSOC). It consisted of twin satellites in a leader/chaser configuration in the same near-circular, near-polar orbit around the Earth. The data provided by the high-precision microwave K/Ka-band ranging (KBR) system between the two satellites proved to be sensitive to mass anomalies on and within the Earth to an unprecedented level not possible before GRACE [1]. This allowed for the time-varying mass distribution of our planet to be much better understood, having profound impact in realms such as groundwater storage, polar ice melt, sea-level rise, currents, ocean heat storage, and surface water hydrology. The mission lasted an astonishing 15 years, providing near-continuous data for estimating Earth's static and time-varying gravity fields. Although the initial mission came to an end in 2017, GRACE Follow-On (GRACE-FO) replaced the two original satellites with upgraded versions, potentially providing even

more precise observations. With a large repository of KBR data, and many years more to come, alternative methods of processing the inter-satellite measurements should be investigated for potential advantages and possibly higher-quality gravity field solutions. This study seeks to accomplish that through assessment of the validity of processing the range-acceleration, the second time derivative of the inter-satellite range, as opposed to the more commonly utilized range-rate.

1.1 GRACE Background

The accurate determination of the Earth's gravity field is necessary for a multitude geophysical sciences, such as oceanography, hydrology, glaciology, and geodesy [1]. Prior to GRACE, estimations of the gravity field had been required to use combinations of years of satellite data with land and sea measurements. The GRACE mission was innovative by now providing a method with which to measure the Earth's gravity field with unprecedented accuracy utilizing only data from a single mission. The two spacecraft in the GRACE/GRACE-FO missions are identical, co-orbiting the Earth in a near-circular and near-polar orbit at a nominal altitude of approximately 500km, with a nominal separation of around 220km [4]. In this configuration, the satellites are able to detect gravitational differences on the planet's surface equivalent to that of a 300-km disk of water only 2-3 centimeters thick [1]. While orbiting the Earth, each of the twin vehicles experience small orbital perturbations primarily induced by the non-uniformity of Earth's gravity field. Due to

their separation in the along-track, these perturbative forces on each satellite differ, resulting in a continuous change of the principal measurement of the GRACE mission, the inter-satellite range. This variation in the inter-satellite range is tracked to very high precision via the dual-frequency, microwave KBR system [2]. Both satellites transmit and receive the dual one-way phase signal in an effort to offset any inherent oscillator-induced errors in the system. Upon transmission of these measurements to a ground processing center, the two signals are combined to produce an ionosphere-free dual one-way range (DOWR), precise to the micron level [1]. The GRACE-FO mission is equipped with an experimental Laser Ranging Interferometer (LRI) as well, with hope of increasing that precision by 1-2 orders of magnitude, or more [1] .

The two satellites are also subject to other gravitational and non-gravitational perturbations, the effects of which must be accounted for in order to produce high-quality gravity field solutions. GRACE-like missions accomplish this through a variety of on-board instruments, as well as the removal of several geophysical process models. For removal of the non-gravitational accelerations on the spacecrafts, they are equipped with SuperStar accelerometers [3]. Additionally, disturbing forces due to solid earth tides, ocean tides, atmospheric and oceanic variability, N-bodies, and relativistic perturbations are taken into account. After removal of these effects from the signal, what remains is indicative of changes in the Earth's gravity field primarily due to surface mass distribution [4]. The KBR data provide a relative measurement

only, and thus, no information about the absolute position and velocity of the two satellites is included. To rectify that, the satellites each possess a highly accurate Blackjack GPS receiver [2], which also provides timing information along the orbit. The two satellites must maintain strict attitude requirements to produce the high-caliber KBR data, which is achieved through on-board star cameras, thrusters, and magnetic torquers. A diagram of the GRACE instrument configuration is provided in Figure 1.1.

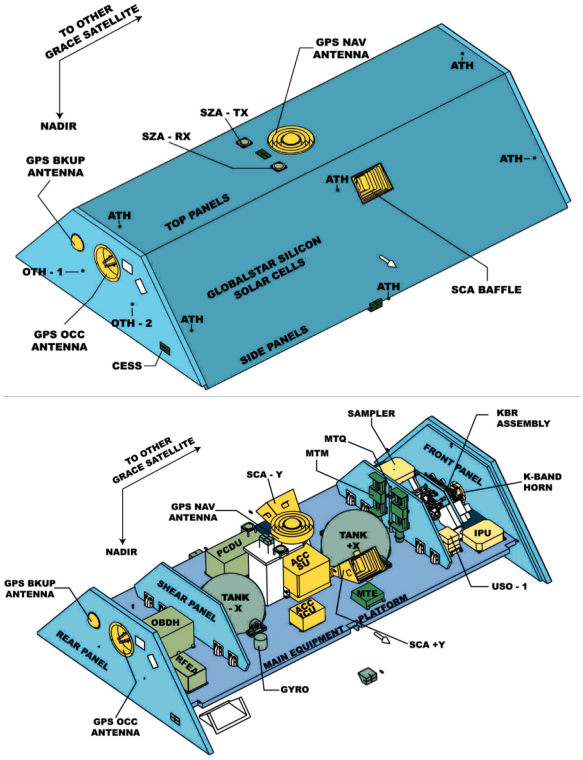

Figure 1.1: GRACE satellite configuration [5]

1.2 Project Motivation and Outline

The purpose of this work, which explores variational methods solely, is to discover and detail what methods, if any, make it possible to generate feasible solutions from the range-acceleration measurements, and to compare them to one obtained based on the range-rate observations. In this study, "variational" methods refer to the use of iterative differential corrections to a vector of global parameters (Stokes coefficients) to ultimately converge on an estimate. Other approaches, such as localized mass concentrations (mascons), are outside the scope of this research and may exhibit dissimilar behavior. This thesis does not attempt to develop a methodology in which the range-accelerations guarantee a better solution than the range-rate (although that could be a recommendation for future study), but explores whether or not the idea of range-acceleration based solutions is even viable with a variational approach. Motivation for this stems from the fact that there exists a theoretical possibility that the range-acceleration signal contains higher-resolution gravity signal and in turn may result in an improvement in the North-South striping error typical of range-rate based gravity field solutions. This has been investigated by Tregoning [7], in which a benefit was found through utilization of smoothed range-accelerations to produce a mascon representation of the gravity field. This work seeks similar improvements, albeit in the spherical harmonic representation of the gravity field, which will be detailed in the next chapter. Chapter 2 contains an overview of the mathematical formulation for

GRACE-like gravity field solutions, which includes the previously mentioned representation of the gravity field, the nonlinear estimation theory which enables solving for it from the KBR observations, and a general description of how this is implemented at CSR. Chapter 3 details the analytical derivation of the range-acceleration observation model for the GRACE mission, as well as a validation of its partial derivatives. Gravity field solutions from status quo range-acceleration processing are shown to be far inferior to those of range-rate. This motivates validation of the various error sources used to simulate the range-acceleration data, as well as a solution vs. error sensitivity study. Chapter 4 explores the CRN-filter, the current method of obtaining the range-acceleration pseudo-observations from the KBR data and attempts to tune it for range-acceleration based solutions. An alternative, more noise-robust method is presented as well. Chapter 5 applies a new technique, first suggested by Tregoning [8], to the spherical harmonic domain and achieves considerably improved solutions. Finally, Chapter 6 will summarize the results of the study and state conclusions drawn from the work.

Chapter 2

GRACE Mathematical Formulation

The concept behind the GRACE mission is rather ingenious in its formulation. This chapter is intended to give a high-level overview of how the precision measurements of the two satellites are able to produce the high-quality estimates of Earth's gravity field. The explicit derivations of these fundamental background theories have been extensively well-covered in other works, such as Kaula [24] and Tapley [12], thus only a basic sketch of the concepts are provided here, without explicit detail.

2.1 Gravity Field Representation

2.1.1 The Geoid

In the Newtonian limit, gravity can represented as a force (or negative gradient of a potential) of mutual attraction between two objects, and the gravitational potential of a body can be formulated via a three-dimensional integral of its mass density over its volume. The gravitational potential, U, of a differential volume element, dV, at point $\boldsymbol{r}$, in Cartesian coordinates, is represented by the following expression:

$$U(\boldsymbol{r}) = G \int \int \int_V \frac{\rho(\boldsymbol{r'})}{|\boldsymbol{r} - \boldsymbol{r'}|} dV \tag{2.1}$$

There are two things that need to be addressed here. The first being that there exists no analytical formula for the Earth's density, therefore the triple integral is not possible to calculate, and some other way to represent the field mathematically must be used. This will be dealt with shortly. The second is that the gravity field exists everywhere, at every point extending to infinity, so in discussing the potential in any meaningful way it is necessary to specify a reference location. This latter issue is resolved by referring to Earth's gravitational potential, the geopotential, in terms of an equipotential surface, or a surface of constant value. The most significant and conventionally-used equipotential surface of reference for Earth is known as "the geoid", which is the surface that would be described by the mean sea level (MSL), if the oceans and atmosphere were in equilibrium and at rest relative to the rotating Earth. A diagram depicting the geoid is shown in Figure 2.1.

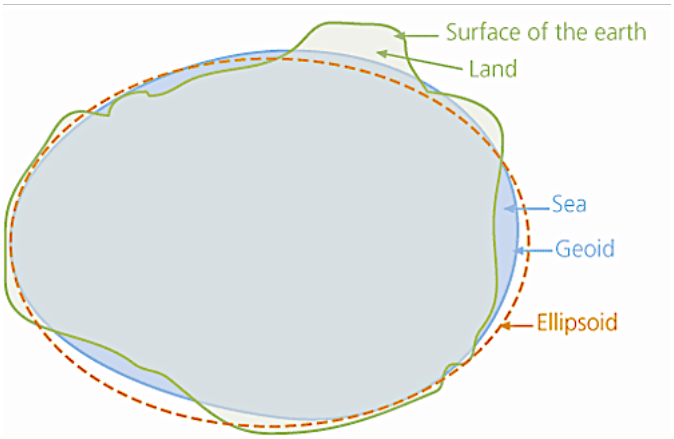

Figure 2.1: Diagram of the geoid
[http://www.esri.com/news/arcuser/0703/geoid1of3.html]

In this research, a "gravity field solution" is a mathematical description for Earth from which the geoid can be resolved, leading to the first issue.

2.1.2 Spherical Harmonics

As previously mentioned, the triple integral in Equation 2.1 is not directly calculable and necessitates another mathematical formulation to represent the geopotential. Transformation of the geopotential follows the procedure laid out by Kaula [24], and involves first representing the triple integral in spherical coordinates r, ϕ, and λ. Then, separation of variables can be used to find solutions to Equation 2.2, Laplace's equation.

$$\nabla^2 U = 0 \tag{2.2}$$

The outcome of this process results in the geopotential's expansion into a summed infinite series of spherical harmonics, which takes the following form in the Earth-fixed reference frame:

$$U(r,\phi,\lambda) = \frac{\mu}{r} + \frac{\mu}{r}\sum_{l=2}^{\infty}\sum_{m=0}^{l}\left(\frac{R_e}{r}\right)^l \overline{P}_{lm}(\sin\phi)(\overline{C}_{lm}\cos m\lambda + \overline{S}_{lm}\sin m\lambda) \tag{2.3}$$

where,

μ = Earth's gravitational parameter (GM),

R_e = mean radius of the Earth,

r = radial position of the satellite,

ϕ = geocentric latitude of the satellite,

λ = geocentric longitude of the satellite,

l = spherical harmonic degree,

m = spherical harmonic order,

$\overline{P}_{lm}$ = normalized associated Legendre polynomials,

$\overline{C}_{lm}/\overline{S}_{lm}$ = normalized spherical harmonic (Stokes) coefficients.

The $l = 1$ term is neglected as the origin of the coordinate frame is assumed to coincide with the center of mass of the Earth. Missions involving study of the geopotential focus on the second term of Equation 2.3, which represents the non-trivial, non-spherical portion of the potential. It should be noted that the spherical harmonic representation of the gravity field is a "global" one, meaning that local gravity signals and errors could be propagated over the entire globe [28]. Other gravity field representations, such as mascons, often prove better at localizing particular signals in the gravity field over a certain region. Throughout this thesis, the spherical harmonic representation is used in order to model the gravity field globally. In this research, a data span of 31 days, the entire month of August 2008, was chosen to ensure global ground-track coverage by the two satellites.

2.1.3 Relevance to GRACE

The Earth's gravitational potential is variable over time due to the redistribution of mass by processes such as seasonal weather, polar ice melt, and seismic activity. Therefore the Stokes coefficients of the gravity field are not static, but consist of both a mean and time-variable portion as shown in Equation 2.4.

$$\begin{aligned} \overline{C}_{lm}(t) &= \overline{C}^{0}_{lm} + \Delta\overline{C}_{lm}(t) \\ \overline{S}_{lm}(t) &= \overline{S}^{0}_{lm} + \Delta\overline{S}_{lm}(t) \end{aligned} \tag{2.4}$$

It is the estimate of these coefficients that are the final "gravity field solutions", or Level-2 products, from the processing of GRACE satellite-to-satellite tracking (SST) measurements [20]. They contain a time-series of the monthly time-variable and mean gravity fields. The coefficients represent the global structure of the gravity field, where higher degree and order correspond to higher frequencies and higher spatial resolution. While the theoretical formulation extends the series to infinity, the actual solutions must be truncated for practical and computational reasons. Typically, the solutions produced at CSR range in degree from 60-96. In this study of the range-accelerations, solutions were carried out to degree and order (d/o) 180 in order to assess the possibility of those measurements improving spatial resolution of the gravity field estimates.

GRACE-like missions make these particular solutions possible by connecting the equations of motion of the satellites to the SST measurements provided by the KBR instrument. The differential equation governing the motion of an Earth-orbiting satellite is as follows:

$$\ddot{\boldsymbol{r}} = \boldsymbol{a_g} + \boldsymbol{a_{ng}} \tag{2.5}$$

where,

$\ddot{\boldsymbol{r}}$ = acceleration of the satellite,

$\boldsymbol{a_g}$ = accelerations due to the mean mass distribution of the Earth,

+ accelerations due to solid Earth tides,

+ accelerations due to ocean tides,

+ accelerations due to atmospheric and oceanic variability,

+ accelerations due to n-bodies,

+ accelerations due to general relativity,

$\boldsymbol{a_{ng}}$ = accelerations due to non-gravitational forces.

The $\boldsymbol{a_{ng}}$ term refers to the sum of all the non-gravitational, non-conservative forces acting on the spacecraft throughout its orbit. These include atmospheric drag, SRP, Earth albedo, thermal radiation, thrusts, and others. These effects are removed from the estimation of the satellites' orbits using the onboard accelerometer measurements. The perturbations in $\boldsymbol{a_g}$, however, are gravitational (conservative) and not sensed by the accelerometers. Some contribu-

tions to $\boldsymbol{a_g}$, which are lumped into $\boldsymbol{a_{geo}}$ in Equation 2.6, can be represented as the gradient of a spherical harmonic potential (the static field, tides, atmosphere/ocean variations). Those remaining, such as planetary perturbations and relativity, are calculated otherwise.

$$\boldsymbol{a_{geo}} = \nabla U \tag{2.6}$$

The $\boldsymbol{a_{geo}}$ term is delineated further still, into components which are known and those which are adjusted. The known components are referred to as the "background" gravity model, and have their effects accounted for via models, each of which are detailed in Bettadpur [16],[21]. The adjusted parameters are represented by deltas on the spherical harmonic coefficients as seen in Equation 2.4.

The only remaining piece is to connect the KBR measurements to the variation in $\boldsymbol{a_{geo}}$ experienced by the satellites due to their along-track separation. The measurement equation for the range-rate achieves this through the variational equations [11], whereas the range-acceleration equation contains this difference in acceleration directly.

2.2 Batch Least Squares Estimation

Full derivation of the tenets of estimation theory are widely available from other sources, such as Tapley [12], and are not reproduced here. This section is meant to provide a basic understanding of how noisy SST measure-

ments from GRACE-like missions are used to achieve an estimate of Earth's gravity field coefficients. While many other methodologies exist, this work uses the variational equations and adjusts the estimate via an iterative, linearized batch least squares (BLS) algorithm.

2.2.1 State Vector and Observation Model

The state vector, $\boldsymbol{X}$, consists of all the variables/parameters to be estimated in the dynamical system and is typically represented as shown in Equation 2.7.

$$\boldsymbol{X} = [\boldsymbol{r}\ \boldsymbol{v}\ \boldsymbol{\alpha}]^T \tag{2.7}$$

where,

$\boldsymbol{r}$ = positions of the satellites,

$\boldsymbol{v}$ = velocities of the satellites,

$\boldsymbol{\alpha}$ = other parameters to be estimated such as gravity coefficients and accelerometer biases/scale factors,

The relationship between the state to be estimated and the observation vector, $\boldsymbol{Y}$, is expressed as

$$\boldsymbol{Y}_i = \boldsymbol{G}(\boldsymbol{X}(t_i), t_i) + \boldsymbol{\epsilon}_i \tag{2.8}$$

where,

$\boldsymbol{Y}_i$ = observation at time t_i,

$\boldsymbol{G}(\boldsymbol{X}(t_i), t_i)$ = nonlinear function of the true state at time t_i,

$\boldsymbol{\epsilon}_i$ = observation errors.

The mathematical models for the KBR observations are highly nonlinear in nature and in order to transform the nonlinear estimation problem into a tractable linear one, it is necessary to linearize the equations about a nominal reference model. Then, the state vector which is to be solved for consists of deviations from this nominal. This is shown in Equations 2.9 and 2.10,

$$\boldsymbol{x}(t) = \boldsymbol{X}(t) - \boldsymbol{X}^*(t) \tag{2.9}$$

$$\boldsymbol{y}(t) = \boldsymbol{Y}(t) - \boldsymbol{Y}^*(t) \tag{2.10}$$

where,

$\boldsymbol{Y}(t)$ = observation vector,

$\boldsymbol{Y}^*(t)$ = calculated reference observation vector,

$\boldsymbol{y}(t)$ = deviation vector between observations and reference observations,

$\boldsymbol{X}(t)$ = unknown, true state vector,

$\boldsymbol{X}^*(t)$ = reference state vector,

$\boldsymbol{x}(t)$ = deviation vector between true and reference state,

The solution for $\boldsymbol{y}(t)$ can be found by linearizing about the reference model via Taylor expansion, given by,

$$\boldsymbol{Y}^*(t) + \boldsymbol{y}(t) = \boldsymbol{G}(\boldsymbol{X}^*(t) + \boldsymbol{x}(t), t) + \boldsymbol{\epsilon} = \boldsymbol{G}(\boldsymbol{X}^*(t), t) + \left[\frac{\partial \boldsymbol{G}}{\partial \boldsymbol{X}}\right]^* \boldsymbol{x}(t) + O(\boldsymbol{x}^2(t)) + \boldsymbol{\epsilon} \tag{2.11}$$

where,

$$[]^* = \text{evaluation at the reference values.}$$

Dropping the higher-order terms and subtracting the reference values gives the linearized observation equations expressed in Equation 2.12,

$$\boldsymbol{y_i} = \tilde{\boldsymbol{H}}_i \boldsymbol{x}(t_i) + \boldsymbol{\epsilon}_i \tag{2.12}$$

where,

$$\tilde{\boldsymbol{H}}_i = \left[\frac{\partial \boldsymbol{G}}{\partial \boldsymbol{X}}\right]_i^*$$

This linearization, as well as that of the dynamics shown in the following section, will form a linear system of equations, which is then solvable.

2.2.2 Dynamics, and the State-Transition Matrix

In the dynamical system, the evolution of the state is governed by dynamical models that are a function of the state itself, expressed as,

$$\dot{\boldsymbol{X}} = \boldsymbol{F}(\boldsymbol{X}, t) \tag{2.13}$$

where,

$\dot{\boldsymbol{X}}$ = change in state over time,

$\boldsymbol{F}(\boldsymbol{X}, t)$ = dynamical models governing evolution of state

A Taylor series approximation of Equation 2.13 can allow linearization of this expression as well. This is shown in Equations 2.14 and 2.15.

$$\dot{\boldsymbol{X}}^{*}(t) + \dot{\boldsymbol{x}}(t) = \boldsymbol{F}(\boldsymbol{X}^{*} + \boldsymbol{x}, t) = \boldsymbol{F}(\boldsymbol{X}^{*}, t) + \left[\frac{\partial \boldsymbol{F}(t)}{\partial \boldsymbol{X}(t)}\right]^{*} \boldsymbol{x}(t) + O(\boldsymbol{x}^{2}(t)) \tag{2.14}$$

where,

$\dot{\boldsymbol{x}}(t)$ = change in deviation vector over time,

$[]^{*}$ = evaluation at the reference values.

By dropping the higher-order terms and subtracting the reference evaluation this equation becomes,

$$\dot{\boldsymbol{x}}(t) = \boldsymbol{A}(t)\boldsymbol{x}(t) \tag{2.15}$$

where,

$$\boldsymbol{A}(t) = \left[\frac{\partial \boldsymbol{F}(t)}{\partial \boldsymbol{X}(t)}\right]^{*}$$

The general solution to Equation 2.15 is given as,

$$\boldsymbol{x}(t) = \boldsymbol{\Phi}(t, t_0)\boldsymbol{x}(t_0) \tag{2.16}$$

where,

$$\boldsymbol{\Phi}(t, t_0) = \left[\frac{\partial \boldsymbol{X}(t)}{\partial \boldsymbol{X}(t_0)}\right],$$

$$= \text{state-transition matrix (STM) from } t_0 \text{ to time } t,$$

$$\boldsymbol{x}(t_0) \quad = \boldsymbol{x}_0 = \text{state deviation evaluated at the initial epoch.}$$

The full properties of the STM are derived and provided in Tapley [12], however it satisfies the differential equation given in Equation 2.17,

$$\dot{\boldsymbol{\Phi}}(t, t_0) = \boldsymbol{A}(t)\boldsymbol{\Phi}(t, t_0) \tag{2.17}$$

with initial conditions,

$$\boldsymbol{\Phi}(t_0, t_0) = \boldsymbol{I} \tag{2.18}$$

where,

$$\boldsymbol{I} = \text{the identity matrix.}$$

Numerical integration is then required to obtain the STM at any time, t.

2.2.3 System of Equations and Solution

By substituting Equation 2.16 into Equation 2.12, the transformation of the problem into a system of linear equations mapping the observations to the initial epoch is complete. They are stacked and expressed as,

$$\begin{bmatrix} y_1 \\ y_2 \\ \vdots \\ y_m \end{bmatrix} = \begin{bmatrix} y_1 \\ y_2 \\ \vdots \\ y_m \end{bmatrix} \begin{bmatrix} \tilde{\boldsymbol{H}}_1 \boldsymbol{\Phi}(t_1, t_0) \\ \tilde{\boldsymbol{H}}_2 \boldsymbol{\Phi}(t_2, t_0) \\ \vdots \\ \tilde{\boldsymbol{H}}_m \boldsymbol{\Phi}(t_m, t_0) \end{bmatrix} \begin{bmatrix} x_1 \\ x_2 \\ \vdots \\ x_n \end{bmatrix} + \begin{bmatrix} \epsilon_1 \\ \epsilon_2 \\ \vdots \\ \epsilon_m \end{bmatrix} \tag{2.19}$$

or finally, in condensed form,

$$\boldsymbol{y} = \boldsymbol{H}\boldsymbol{x} + \boldsymbol{\epsilon} \tag{2.20}$$

where,

$\boldsymbol{y}$ = $m \times 1$ vector of measurement deviations,
observed minus computed $(O - C)$,

$\boldsymbol{H}$ = $m \times n$ matrix mapping observations to initial epoch,

$\boldsymbol{x}$ = $n \times 1$ vector of unknown deviation from reference state,

$\boldsymbol{\epsilon}$ = $m \times 1$ vector of errors.

The error vector, ϵ, represents the accumulation of all errors involved in the formulation, which includes neglect of higher-order terms, integration errors, errors in dynamic models, systematic noise, measurement noise, etc.

The solution to this system may be computed in several different ways, depending on application. Due to the very large numbers of observations, parameters being estimated, and ill-conditioning of the system in GRACE-like

missions, more computationally efficient methods involving regularization and orthogonal transformations such as QR decomposition are generally employed. However, the most straightforward solution is provided by the normal equations. They are provided here for reference, but a comprehensive derivation can be found in Tapley [12]. The solution for the estimate of the deviations to the reference state, $\hat{\boldsymbol{x}}$, is given by the weighted least squares solution in the following form,

$$\hat{\boldsymbol{x}} = (\boldsymbol{H}^T \boldsymbol{W} \boldsymbol{H})^{-1} \boldsymbol{H}^T \boldsymbol{W} \boldsymbol{y} \tag{2.21}$$

where,

$$\boldsymbol{W} = \text{weighting matrix for the observations.}$$

If it is assumed that the measurement errors are independent and have zero mean, making the measurement error covariance matrix, $\boldsymbol{R}$, a diagonal matrix, then its inverse can be used for the weighting matrix to achieve the minimum variance solution,

$$\hat{\boldsymbol{x}} = (\boldsymbol{H}^T \boldsymbol{R}^{-1} \boldsymbol{H})^{-1} \boldsymbol{H}^T \boldsymbol{R}^{-1} \boldsymbol{y} \tag{2.22}$$

The $(\boldsymbol{H}^T \boldsymbol{R}^{-1} \boldsymbol{H})^{-1}$ matrix is known as the variance-covariance matrix and determines the level of confidence in the solution. The terms along the diagonal of this matrix provide the uncertainties in the resultant estimated parameters at each iteration, while the off-diagonal terms are the covariances of the parameters multiplied by their respective correlation coefficient. It is possible

to augment this problem with prior knowledge of the system and include an *a priori* covariance matrix, generally denoted as $\boldsymbol{P}$. The solutions in this research do not include any *a priori*, and while this does lead to noisier estimates of the gravity field, the resulting solution is less constrained.

2.2.4 Relevance to Gravity Field Estimation

Using this linearized system and the KBR measurements from the GRACE satellites, one is able to implement a solution algorithm to arrive at the desired end product, which is a vector of Stokes coefficient deviations, ΔC_{nm} and ΔS_{nm}, to the gravity field model used for reference. In this research, the GRACE Intermediate Field 48 (GIF48) was used as the nominal field [21]. A basic sketch of the overall solution process follows.

2.2.4.1 Orbit Determination

The SST observations of the GRACE mission are, precise as they may be, relative measurements only. They provide no information about the absolute positions or velocities of the two spacecraft. To solve this, GRACE-like missions employ GPS receivers onboard to obtain High-Low Satellite-to-Satellite (HL-SST) measurements from the GPS constellation to determine their orbits.. The observation models for acceleration, shown in the next chapter, require the relative velocity vector between the two satellites, which can only be determined from the HL-SST observations. The GPS tracking measurements are formulated into an orbit determination problem of their own,

and this is iterated to achieve a best-fit orbit comprised of the positions and velocities of the two satellites over the data arc.

2.2.4.2 Partial Derivatives and Residuals (Regress Files)

In order to form the very large measurement mapping matrix, $\boldsymbol{H}$, the equations of motion (Equation 2.5) need to be numerically integrated and the measurement partial derivatives with respect to each state variable/parameter, $\frac{\partial \boldsymbol{G}}{\partial \boldsymbol{X}}$ need to be computed as well. In the case of the range-accelerations, this is an especially herculean task, as the spherical harmonic series shows up twice in the measurement equation itself and contains ∼32,000 terms at each timestep for d/o 180. The observation residual vector, $\boldsymbol{y}$, is also calculated by subtracting the computed observations from the observed ones ($O-C$). These are written out into files known as regress files along with the $\boldsymbol{H}$ matrix. The software utilized to carry out this step and the one prior is the Multi-Satellite Orbit Determination Program (MSODP) from CSR [17].

2.2.4.3 Solution of the Linear System

With the two previous steps completed, all that remains is to perform the linear algebra for the solution equation to obtain an estimate of the satellite initial conditions, Stokes coefficients, accelerometer scale factors/biases, and any other parameters included in the state vector. This calculation is accomplished via the Advanced Equation Solver for Parallel Systems (AESoP) from CSR [18]. The two different data sets, GPS and KBR, are given relative

weights to influence how much the solution trusts those particular measurements. The GPS data weights are a heuristic input, while the KBR weights are a ratio of user input measurement standard deviations to the actual standard deviation of the measurement residuals and allowed to adjust.

For this research, both MSODP and AESoP were deployed on the Lonestar 5 supercomputer at the Texas Advance Computing Center (TACC) due to the parallel processing requirements of the problem.

2.3 Assessment of Gravity Field Solution Quality

Since this study aims to compare gravity field solutions output from varied processing techniques, it is necessary to understand the metrics by which they can be evaluated and contrasted against one another. This section outlines the primary modes of gravity field quality assessment which enable characterization of the errors and uncertainties in the solution coefficients. For consistency, experimental range-acceleration solutions from simulated data will be measured against a single "good" solution, here after referred to as the "baseline solution". The baseline solution used in this research is a simulation for the month of August 2008, processed via the typical range-rate observations. The range-rate measurements produced for the baseline solution were done so via the currently used 100mHz passband CRN-filter, detailed in Section 4.2. The error assumptions for both the baseline solution and range-acceleration experiments in this research are described in the next chapter.

2.3.1 Spherical Harmonic Solution Statistics

The main method of examining differences between solutions comes from the error statistics of the spherical harmonics coefficients. Two different metrics are described, and it is explained that these relate to the concepts of precision and accuracy of the gravity field solutions.

2.3.1.1 Degree Error Variance

Any solution to an estimation problem requires an associated confidence level to be meaningful. In the formulation of GRACE, this information comes via the error variances which form the output covariance matrix from the least squares solution. The degree error variance (DEV) of the n^{th} degree is defined as follows,

$$\delta_n = \sqrt{\sum_{m=0}^{n} (\delta \overline{C}_{nm}^2 + \delta \overline{S}_{nm}^2)} \tag{2.23}$$

where,

$$\delta \overline{C}_{nm},\ \delta \overline{S}_{nm} = \text{standard deviation of the errors in the estimates of the normalized Stokes coefficients.}$$

The degree error variance is proportional to measurement noise, and thus to the relative weighting factors provided to, or calculated by, AESoP during the solution process. Additionally, correlation of the parameter errors is neglected, producing an optimistic view of the overall error. The DEV is analogous to the

precision of the estimate, providing no insight into how accurate the solution may be.

2.3.1.2 Degree Difference Variance

In the case of simulations, where the true gravity field being estimated is actually known, an additional comparison metric is available. The degree difference variance (DDV) is the difference between the reference and estimated spherical harmonic coefficients, and is defined as follows,

$$\Delta_n = \sqrt{\sum_{m=0}^{n} (\Delta \overline{C}_{nm}^2 + \Delta \overline{S}_{nm}^2)} \tag{2.24}$$

where,

$$\Delta \overline{C}_{nm} = (\overline{C}_{nm})_{\text{estimated}} - (\overline{C}_{nm})_{\text{reference}}$$
$$\Delta \overline{S}_{nm} = (\overline{S}_{nm})_{\text{estimated}} - (\overline{S}_{nm})_{\text{reference}}$$

For solutions utilizing real observations from the mission, the true gravity field is unknown and only the DEV is available for comparison, unless other external metrics are included. However, in the case of simulations, the DDV represents an actual error metric and is also less sensitive to the data measurement weighting factors, therefore it is a better quantity for evaluating solutions using simulated data. The DDV is analogous to the accuracy of the estimate, indicating how far away from the truth a particular solution lies.

2.3.1.3 Graphical Representations

There exist several convenient visualizations for the spherical harmonic statistics, and depending on the type of analysis, any one or all three may be used. These are the DDV/DEV plots, triangles plots, and world maps depicting gravity anomalies mapped onto the globe.

DDV/DEV Plots

Both the DDV and DEV are typically scaled up by R_e, the mean radius of the Earth, in order to represent their contribution to the error in geoid height. Typically a plot is made of geoid height error on a logarithmic scale vs. degree for visual representation of the errors. A DDV/DEV plot for the baseline solution is shown in Figure 2.2. Again, here the term "baseline solution" refers to the range-rate solution from simulated August 2008 measurements. Also present on the figure are the GIF48 reference DEV, as well as the baseline and reference degree variance (DV), which are simply the gravity coefficients themselves, summed by degree. This visualization serves as the primary method of comparing various gravity field solutions.

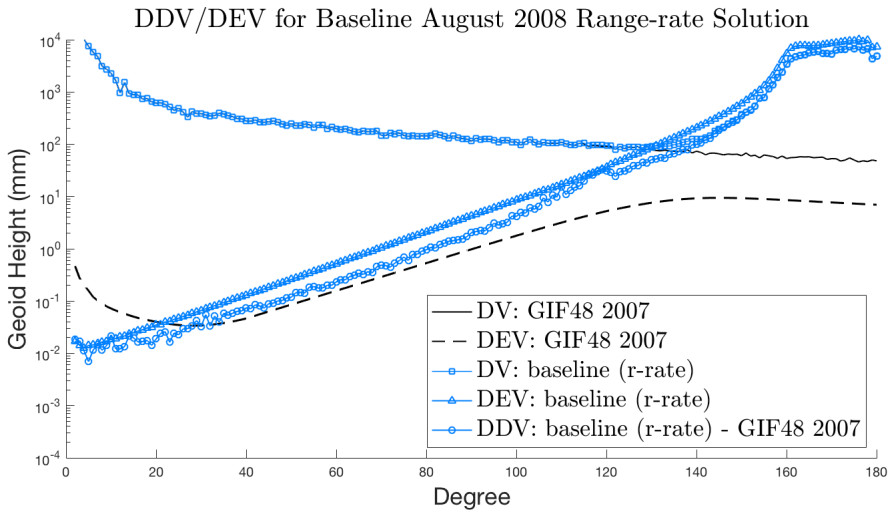

Figure 2.2: DDV/DEV plot for the Aug 2008 baseline solution

The DV (blue squares) of the baseline solution tracks closely with that of the truth field up to approximately degree-110, and the DDV (blue circles) indicate that the per-degree geoid height errors up to that point are less than 10mm. From there, the errors start to grow substantially, and by degree-130, the results begin to diverge from the truth completely. These features create a benchmark against which the range-acceleration solutions can be compared. DV curves which match that of the GIF48 reference field up to higher degrees, and consequently DDV curves which appear lower on the plot than those shown here, indicate improvement in that particular solution over the baseline.

Triangle Plots

The DDV/DEV plots are extremely informative about the quality of an output solution, particularly when it comes to simulations, but there is a large amount of detail that is abandoned in order to plot the cumulative error by degree only. All specifics regarding harmonic order are summed into a single number, only leaving what is essentially a two-dimensional cross-section of a three-dimensional metric. Triangle plots are a tool for overcoming this limitation of the previous plot. In essence, it is a bird's-eye view, colored elevation map, allowing the observation of geoid height error contributed by each individual degree and order. Each degree is broken down into its order constituents, indexed by m, and of which there are typically $n + 1$ of them for each degree n. A color scale is chosen in which one end of the spectrum represents the lowest error values, and conversely, the other end represents the much larger error contributions. For this thesis, a cool-to-hot scale is used, where hotter colors indicate larger errors. The triangle plots for the baseline solution DDV and relative DEV are given in Figure 2.3.

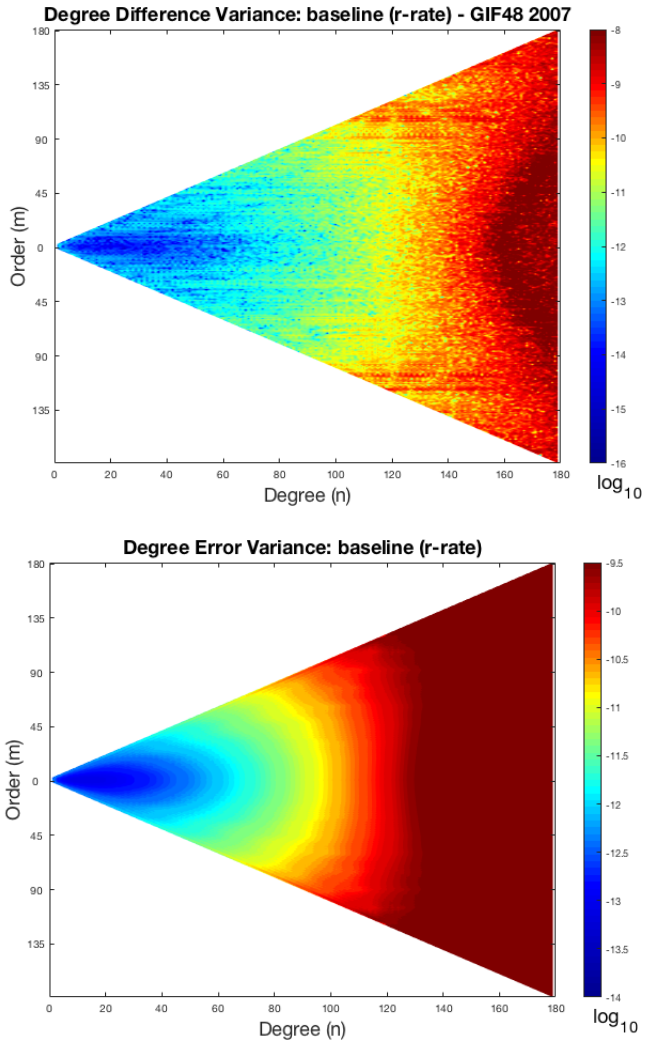

Figure 2.3: DDV/DEV triangle plots for the Aug 2008 baseline solution

The baseline solution produces triangle plots which reinforce and expand upon the information from the DDV/DEV plot. The "cool" color scheme depicts low errors up to approximately degree-110, however it can now be seen that the higher orders are contributing most to the errors at that degree. The overall errors are quite high by degree-150, where the lower orders are then the highest error contributors.

Gravity Anomaly Maps

The GRACE mission is a geodetic study of the Earth and its time varying mass distribution, so visualizing the gravity field in that context provides more insight into the dynamical systems governing the planet and how mass is transported through that system over time. Gravity anomaly maps show how much a particular gravity field solution differs from the gravity field of a uniform, featureless Earth surface. By mapping the gravity field solutions onto a world plot, gravity anomalies are displayed over their corresponding regions, allowing identification for further study and understanding of climate models, earthquakes, polar ice melt, etc. This mapping of the solutions is natural, as the spherical harmonic degrees themselves are representative of physical, spatial wavelengths on the Earth. A relation which connects the two is given by Jean's formula [27] in Equation 2.25, and alternatively, as a heuristic approximation in Equation 2.26,

$$\lambda_n \approx \frac{2\pi}{n+0.5} * R_e \tag{2.25}$$

$$\frac{\lambda_n}{2} \approx \frac{20,000km}{n} \tag{2.26}$$

In this thesis, the gravity anomaly plots depict the variations from the mean of a particular solution and the GIF48 field. This variation for the baseline solution, after having 350km spatial smoothing applied, is plotted on a world map in Figure 2.4.

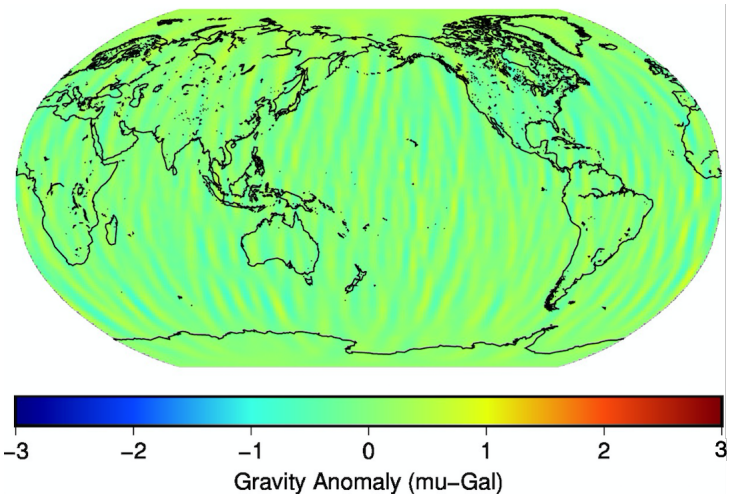

Figure 2.4: Gravity anomaly map for the Aug 2008 baseline solution

A very consistent, almost uniform color would be an indication of near-perfect agreement between the estimated and the true gravity fields. To clarify, if the two solutions compared are closely matched, then their mean does not deviate substantially from either solution, and very little color variance would be displayed on the plot. There are anomalies present in the baseline solution however, manifesting as the typical North-South striping errors which plague

gravity field solutions and are not representative of real gravity signal. These stripes represent errors in the data processing and/or gravity field estimation process, as there exists no real, physical Earth feature or phenomenon which would create such a signal. It appears the maximum magnitude of the anomalies present here, according to the color scale, is approximately 1μGal, where $1\mu\text{Gal} = 10\frac{nm}{s^2}$. This is the value against which range-acceleration anomalies will be evaluated.

2.3.2 Measurement Post-fit Residuals

The measurement residuals which remain after the estimation process can divulge a wealth of information about the solution and the processing methodology. The post-fit residuals, analyzed in the time domain, indicate how well the computed observation models match the measurements of the satellites. Ideally, these are quite "small" in magnitude, and have a zero-mean, flat signature representative of random noise. Any other mean value or signature would be a clear indicator of mismodeling.

When transformed into the frequency domain, via Fourier Transform, the power of each frequency contained in the signal can be revealed. The power vs. frequency plot is known as the power spectral density (PSD) of the signal. Hopefully, most of the gravity signal has been accounted for by the solution, leaving only noise behind. There is, however, an upper limit on both frequencies of interest, as well as what the satellites can sense given their spa-

tial resolution and instrument precision limits. To approximate the maximum frequencies of relevance in a gravity field of degree n, Equation 2.25 can be applied. This rule approximates the wavelength, λ_n, of the signal at degree-n.

For simplicity, if we assume a circular orbit for GRACE at 500km, and desire the solutions to be carried out to degree-180, the approximate signal wavelength is ∼222km, and the corresponding frequency ∼34mHz. Realistically, the SNR at this high frequency is too degraded to be of much value, but it is used optimistically in this study of the range-accelerations. While CSR does produce monthly solutions up to degree-180 as well, the output coefficients at the higher frequencies contain large errors due to their noise content, so typically the gravity signal of interest has an upper limit of ∼0.18mHz, which coincides with degree-96.

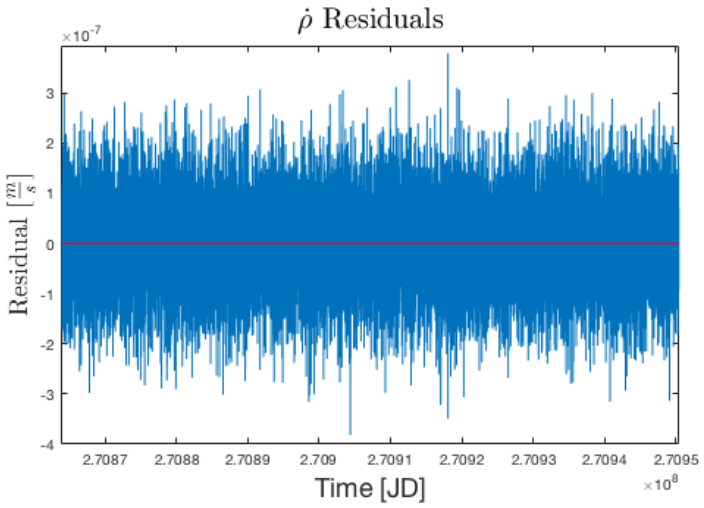

Figure 2.5: Time domain post-fit residuals, Aug 2008 baseline solution

Figure 2.6 compares the PSD of the simulated measurement noise added to the system against the baseline pre-fit and post-fit KBR residuals. There are notable peaks in the power of the noise and pre-fits at ∼1 cycle-per-revolution (cpr), which are due to systematic and mis/unmodeled force and measurement errors. This signal is removed in the final fit by estimation of periodic empirical parameters, and is not present in the post-fit residuals. The derivation of the expressions which explain the 1-cpr signals is laid out in Kim [5], and is an application of Hill's equations. They show that perturbation of any frequency results in SST perturbations of constant and 1-cpr. Additionally, the PSD of the post-fits remains slightly higher than that of the measurement noise added, indicating there are other corrupting factors aside from those errors alone. Other noise sources, such as the contribution of those simulated errors to the calculation of the "C" (computed measurements) by ACC noise that is integrated into the orbit. This is examined more closely in Chapter 5.

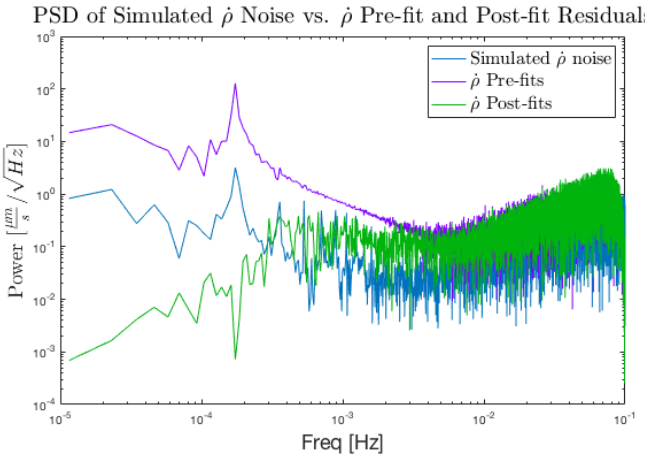

Figure 2.6: PSD of noise vs. pre and post-fit residuals, baseline solution

Chapter 3

Solutions Based on Range-Accelerations

As previously mentioned, the satellite-to-satellite tracking observations of the GRACE mission come in two basic forms; High-Low (HL) and Low-Low (LL). The former refers to measurements taken between the GPS constellation and the two GRACE satellites in order to determine the absolute positions, velocities, and time tags for GRACE-A and GRACE-B. The latter is the KBR measurement taken between the two co-orbiting GRACE spacecrafts, which forms the fundamental measurement of the mission and the one of primary interest in this study. This chapter gives an overview of the analytical formulation for computing the inter-satellite range-acceleration and gravity field estimates arrived at from that processing. The low quality of status-quo gravity field solutions based on range-acceleration is displayed. This necessitates a validation of the noise models which are used to run range-acceleration based simulations and a subsequent study of the solution sensitivity to each noise source is provided.

3.1 Range-Acceleration Model

The range-acceleration between the two spacecraft is a scalar quantity which represents the second time derivative of the continuously changing distance between the two satellites due to the forces on the satellites. The range,

denoted as ρ, is simply the magnitude of the difference in the position vectors of GRACE-A and GRACE-B in the inertial reference frame, given in Equation 3.1.

$$\rho = \sqrt{(\boldsymbol{r}_1 - \boldsymbol{r}_2)^T(\boldsymbol{r}_1 - \boldsymbol{r}_2)} \tag{3.1}$$

where,

$\boldsymbol{r}_{1/2}$ = inertial positions of the leading/trailing satellite, respectively.

Strict pointing requirements for GRACE allow the KBR instruments to maintain a precise line-of-sight (LOS), along which the microwaves are transmitted and received. The LOS vector is defined as the unit vector pointing along the position difference vector from the leading satellite to the trailing, expressed as

$$\hat{\boldsymbol{e}}_{12} = \frac{\boldsymbol{r}_{12}}{\rho} \tag{3.2}$$

where,

$\boldsymbol{r}_{12}$ = relative position vector between the satellites.

Differentiation of the range equation gives the range-rate observable, $\dot{\rho}$,

$$\dot{\rho} = \dot{\boldsymbol{r}}_{12} \cdot \hat{\boldsymbol{e}}_{12} \tag{3.3}$$

which represents the velocity difference vector between the two satellites, $\dot{\boldsymbol{r}}_{12}$, projected onto the LOS vector. An important distinction is that this is not simply the magnitude of the velocity difference vector. A differentiation of the range-rate observable gives the range-acceleration equation, $\ddot{\rho}$, however some rearranging is required to recast it in a form with known quantities from the mission. This is done as follows,

$$\ddot{\rho} = \ddot{\boldsymbol{r}}_{12} \cdot \hat{\boldsymbol{e}}_{12} + \dot{\boldsymbol{r}}_{12} \cdot \dot{\hat{\boldsymbol{e}}}_{12} \tag{3.4}$$

As with the range-rate, the first term projects the acceleration difference vector onto the LOS vector, however there is now an additional term to deal with, which is the product of the velocity difference vector with the LOS rate of change vector, $\dot{\hat{\boldsymbol{e}}}_{12}$. Applying the quotient rule to the LOS vector gives Equation 3.5.

$$\dot{\hat{\boldsymbol{e}}}_{12} = \frac{\dot{\boldsymbol{r}}_{12} \cdot \rho - \boldsymbol{r}_{12} \cdot \dot{\rho}}{\rho^2} \tag{3.5}$$

which, when simplified and dotted with the velocity difference vector, yields the final form of the range-acceleration vector, shown in Equation 3.6,

$$\ddot{\rho} = \ddot{\boldsymbol{r}}_{12} \cdot \hat{\boldsymbol{e}}_{12} + \frac{1}{\rho}(|\dot{\boldsymbol{r}}_{12}|^2 - \dot{\rho}^2) \tag{3.6}$$

The modeled range-acceleration equation contains the difference in gravitational effects on the satellites directly through $\ddot{\boldsymbol{r}}_{12}$ which contains the equations of motion for each satellite (Equation 2.5), and therefore the gradient

of the geopotential. This is projected onto the line-of-sight unit vector in the first term of Equation 3.6. The second term is the centrifugal contribution from the rotation of the inter-satellite baseline.

3.2 Partial Derivatives

While the position and velocity partial derivatives for ρ and $\dot{\rho}$ have relatively simple forms, shown in Equations 3.7-3.10, the range-acceleration partials are much more complicated expressions, as multiple chain-rules and vector derivatives are necessary. Due to their complexity, it seems natural to re-derive these expressions, and then perform their validation using the variational equations. The full derivation is provided in Appendix A.

$$\frac{\partial \rho}{\partial \boldsymbol{r}_1} = \left[\frac{\boldsymbol{r}_{12}}{\rho}\right]^T \qquad \frac{\partial \rho}{\partial \boldsymbol{r}_2} = -\frac{\partial \rho}{\partial \boldsymbol{r}_1} \tag{3.7}$$

$$\frac{\partial \rho}{\partial \dot{\boldsymbol{r}}_1} = 0 \qquad \frac{\partial \rho}{\partial \dot{\boldsymbol{r}}_2} = 0 \tag{3.8}$$

$$\frac{\partial \dot{\rho}}{\partial \boldsymbol{r}_1} = \frac{1}{\rho}\left[\dot{\boldsymbol{r}}_{12} - \frac{\boldsymbol{r}_{12}}{\rho}\dot{\rho}\right]^T \qquad \frac{\partial \dot{\rho}}{\partial \boldsymbol{r}_2} = -\frac{\partial \dot{\rho}}{\partial \boldsymbol{r}_1} \tag{3.9}$$

$$\frac{\partial \dot{\rho}}{\partial \dot{\boldsymbol{r}}_1} = \left[\frac{\boldsymbol{r}_{12}}{\rho}\right]^T \qquad \frac{\partial \dot{\rho}}{\partial \dot{\boldsymbol{r}}_2} = -\frac{\partial \dot{\rho}}{\partial \dot{\boldsymbol{r}}_1} \tag{3.10}$$

3.2.1 Expressions for $\ddot{\rho}$ partials with respect to $\boldsymbol{r}_{1/2}$ and $\dot{\boldsymbol{r}}_{1/2}$

The expressions for the partials are given as follows, with the included simplifying expressions defined after.

$$\frac{\partial \ddot{\rho}}{\partial \boldsymbol{r}_1} = \left[\frac{\partial \ddot{\boldsymbol{r}}_{12}}{\partial \boldsymbol{r}_1}\hat{\boldsymbol{e}}_{12}\right]^T + \frac{1}{\rho}\left[\boldsymbol{h} - \frac{2\dot{\rho}}{\rho}\boldsymbol{c}_{12} - \frac{1}{\rho}|\boldsymbol{c}_{12}|^2\hat{\boldsymbol{e}}_{12}\right]^T$$

$$\frac{\partial \ddot{\rho}}{\partial \boldsymbol{r}_2} = -\left[\frac{\partial \ddot{\boldsymbol{r}}_{12}}{\partial \boldsymbol{r}_2}\hat{\boldsymbol{e}}_{12}\right]^T - \frac{1}{\rho}\left[\boldsymbol{h} - \frac{2\dot{\rho}}{\rho}\boldsymbol{c}_{12} - \frac{1}{\rho}|\boldsymbol{c}_{12}|^2\hat{\boldsymbol{e}}_{12}\right]^T \tag{3.11}$$

$$\frac{\partial \ddot{\rho}}{\partial \dot{\boldsymbol{r}}_1} = \left[\frac{\partial \ddot{\boldsymbol{r}}_{12}}{\partial \dot{\boldsymbol{r}}_1}\hat{\boldsymbol{e}}_{12}\right]^T + \frac{2}{\rho}\boldsymbol{c}_{12}^T$$

$$\frac{\partial \ddot{\rho}}{\partial \dot{\boldsymbol{r}}_2} = -\left[\frac{\partial \ddot{\boldsymbol{r}}_{12}}{\partial \dot{\boldsymbol{r}}_2}\hat{\boldsymbol{e}}_{12}\right]^T - \frac{2}{\rho}\boldsymbol{c}_{12}^T \tag{3.12}$$

where,

$$\boldsymbol{c}_{12} = \dot{\boldsymbol{r}}_{12} - \dot{\rho}\hat{\boldsymbol{e}}_{12}$$

$$\boldsymbol{h} = \ddot{\boldsymbol{r}}_{12} - (\ddot{\boldsymbol{r}}_{12} \cdot \hat{\boldsymbol{e}}_{12})\hat{\boldsymbol{e}}_{12}$$

The fact that these equations contain the accelerations on the satellites, including the spherical harmonic series, makes these partials very computationally expensive, especially for higher d/o solutions. This is one significant drawback to estimation of the gravity field using range-accelerations. In this research, the compute time was amplified by a factor of ∼3-4 for 180x180 solutions over that of range-rate solutions.

3.2.2 Validation of Partial Derivatives

The variational approach was used to assess the correctness of these derived expressions. To do this, a set of initial conditions is used to generate the orbits of the two satellites, GRC-A and GRC-B. At each epoch, the inter-satellite range is produced by differencing the inertial position vectors of the

two satellites. The range-rate and range-accelerations are calculated from the equations of Section 3.1 as well. A small perturbation is introduced to one of the initial conditions, such as GRC-Ax_0 for example, to generate a second set of $\ddot{\rho}$ measurements. The difference in these sets of measurements, $\Delta\ddot{\rho}$, should be approximately equivalent to the partial derivative of the measurement model with respect to the perturbed condition times the initial perturbation, at least in a linear sense for limited period of time. This is shown for the case of an offset in the initial x-coordinate of GRC-A in Equation 3.13.

$$\Delta\ddot{\rho} = \frac{\partial\ddot{\rho}}{\partial GRCAx_0} \cdot \Delta GRCAx_0 \tag{3.13}$$

Validation is performed for the partial derivatives of range-acceleration with respect to (w.r.t.) position and velocity of both GRC-A and GRC-B. Perturbations of 1m in x_0 and $0.1\frac{m}{s}$ in $\dot{x}_0$ were applied to the initial conditions of the two satellites for this study. The following figures display how this initial perturbation mapped to epoch is roughly equal to the difference in SST measurements. The plots are for one full day where the linear approximation still holds fairly well, and the root-mean-square (RMS) error value of the differences over one full day are provided. These values would be even lower if the time span were restricted, to a single orbit for instance.

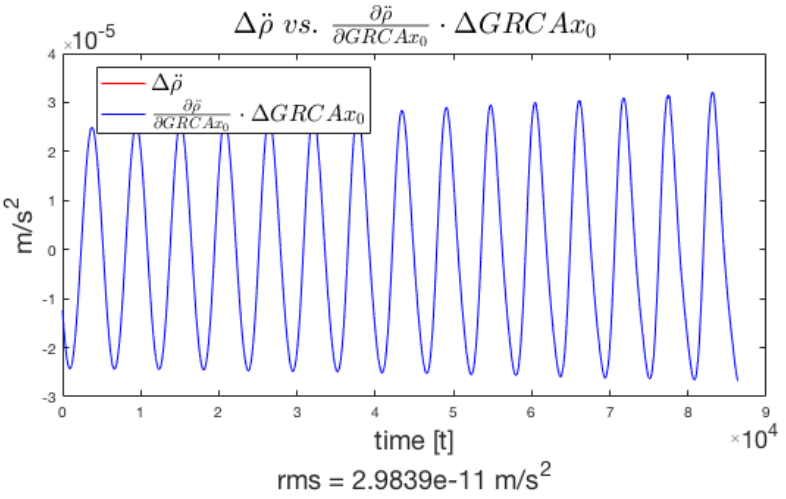

Figure 3.1: Partial w.r.t. GRC-Ax_0

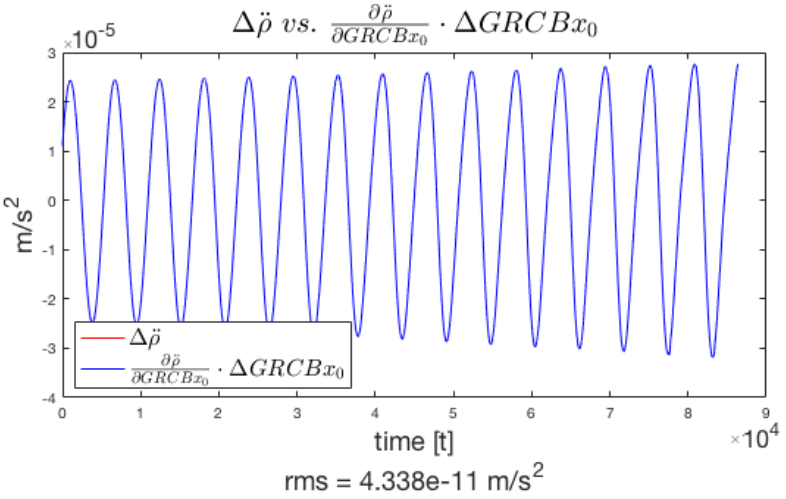

Figure 3.2: Partial w.r.t. GRC-Bx_0

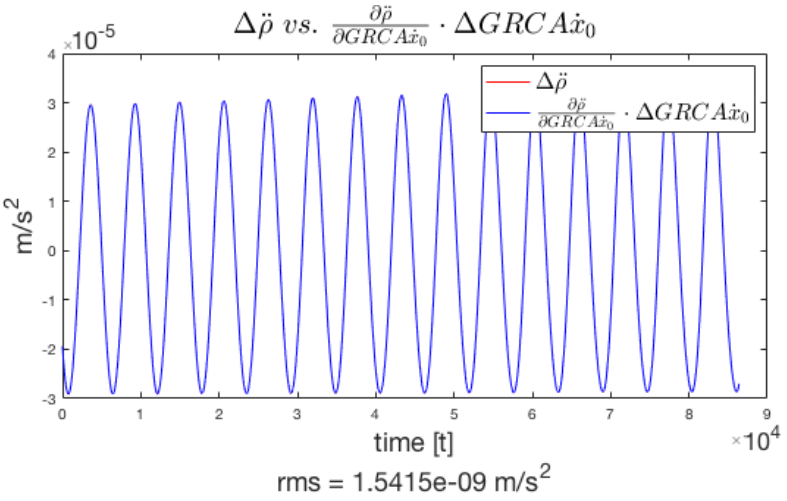

Figure 3.3: Partial w.r.t. GRC-A$\dot{x}_0$

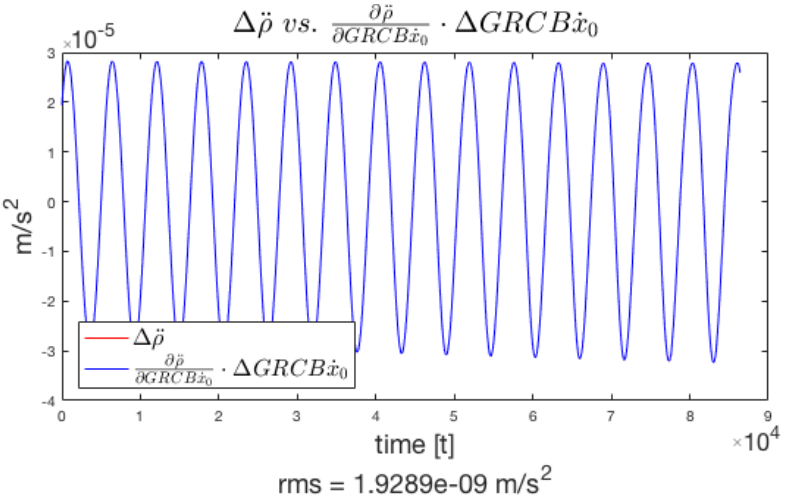

Figure 3.4: Partial w.r.t. GRC-B$\dot{x}_0$

The results of the four test cases are summarized in Table 3.1.

Partial w.r.t	1-Day rms error of partial from truth ($\frac{m}{s^2}$)
GRC-A$_{x_0}$	2.9839e-11
GRC-B$_{x_0}$	4.338e-11
GRC-A$_{\dot{x}_0}$	1.5415e-09
GRC-B$_{\dot{x}_0}$	1.9289e-09

Table 3.1: 1-day rms error for partials

3.3 Status Quo Range-Acceleration Solutions

Theoretically, if the range-acceleration measurements contain more spatially localized, higher-frequency information due to having higher sensitivity in the partials at higher degrees and orders, it should be possible to obtain better estimates of the gravity field at those higher degrees. However, the following figures reveal that simply processing the range-acceleration measurements "as-is" not only does not improve the result, it degrades it by at least an order of magnitude.

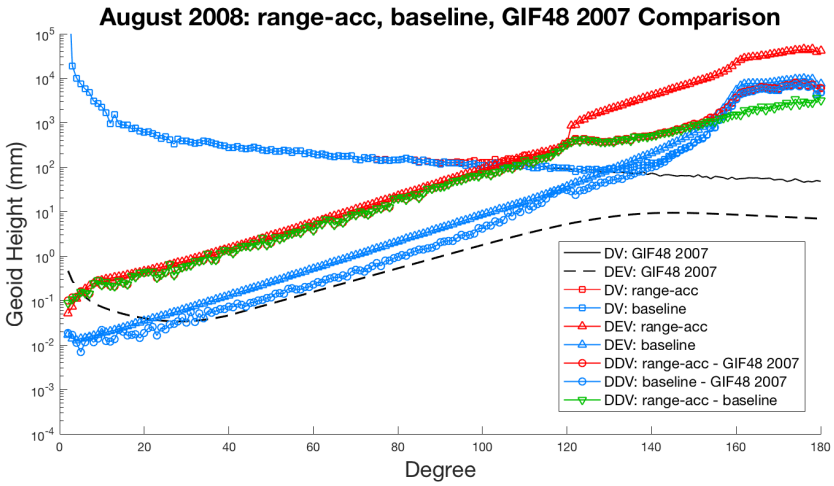

Figure 3.5: DDV/DEV plot for range-acceleration solution vs. baseline

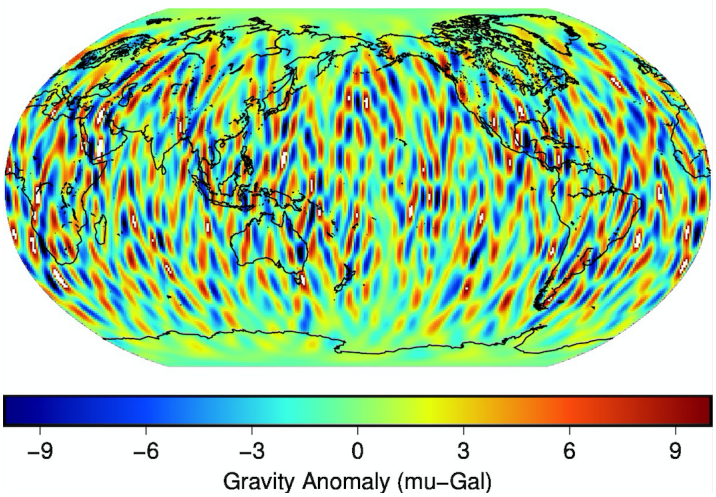

Figure 3.6: Gravity anomaly map for status quo range-acceleration solution

For the anomaly plot, which is spatially smoothed to 350km, the N-S striping errors are much more prevalent than the baseline range-rate solution. The magnitudes of these anomalies outweigh those of the baseline by a factor of

10, necessitating an increase in the plot scale in order to accommodate them. The DDV are degraded by approximately an order of magnitude, with geoid height errors crossing 10mm near degree-70. The DV coefficients themselves start to diverge substantially near degree-90, instead of closer to degree-130 as with the baseline. However, near degree-160, the DDV and DV begin to align with the baseline solution. It is evident that range-acceleration based solutions present a processing challenge to solve.

The simulations in this study provide a testing ground within the current best emulation of the real-world environment of GRACE. Individual elements or models can be adjusted, filtered, or turned on/off completely in an effort to identify the source of the degradation in the range-acceleration solutions. The first and most obvious place to investigate is the simulation setup itself. To examine this, solutions can be generated from noise-free simulated data for both range-rate and range-acceleration. Without the corruption of the measurement noise, both datasets should be able to return a similar solution if all the mechanics are functioning correctly. There are other error sources present in the system, but eliminating the measurement noise, which is by far the most significant, allows for examination of the "minimum-error" case. Figure 3.7 demonstrates the degradation of the solution due to the simulated noise by comparing the baseline range-rate estimate against its minimum-error counterpart. Figure 3.8 shows the similarity of the minimum-error solutions for both range-rate and range-acceleration, which indicates a functioning setup.

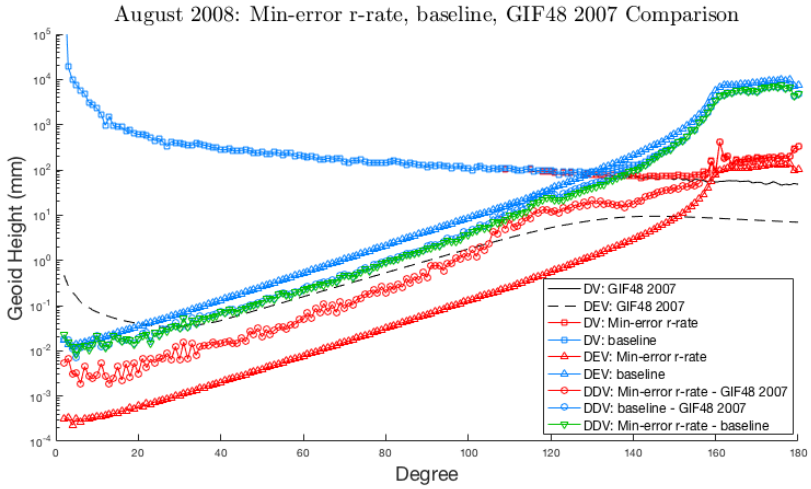

Figure 3.7: DDV/DEV plot for range-rate minimum-error vs. baseline

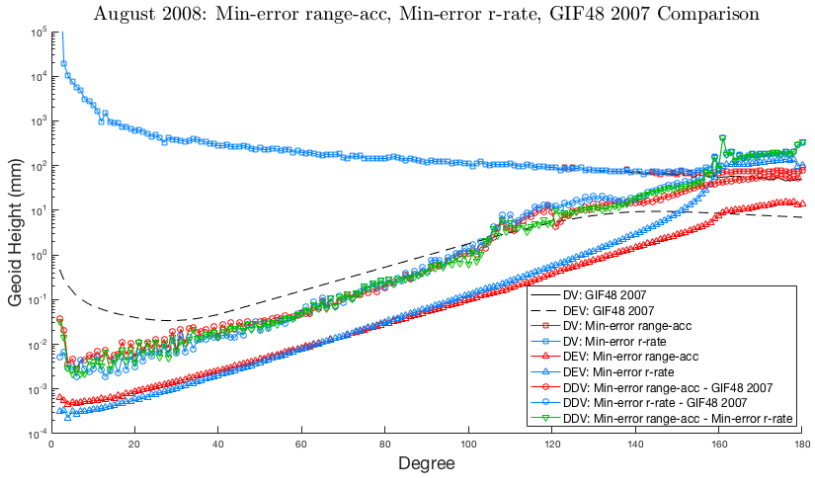

Figure 3.8: DDV/DEV plot for both minimum-error solutions

Figure 3.8 even shows the promise of using range-accelerations for the estimation process, as at the highest degrees those solutions lie closer to the truth. Since the minimum-error setups are in agreement, the error models themselves need to be validated with real data.

3.4 Validation of Noise Models

When running simulations, it is important to have the best understanding possible of the noise sources present in the GRACE system. The basic simulation process is to generate perfect measurements from the truth model, corrupt the data according to these error models, and then attempt recovery of the true gravity field from the imperfect measurements. Estimations from simulated, noisy data can only be meaningful when the simulated noise matches that of reality relatively closely. This section explains the current best estimate (CBE) of the noise contributions to the measurements of GRACE. In order to validate these range-acceleration based simulations, the cumulative resultant noise will be compared against the residuals from real GRACE mission data, which contains the unmodeled signal after processing, or real noise. These models are detailed much more fully in Kim [5], and in general, they are skewed pessimistically in order to overestimate the noise in the system.

3.4.1 Accelerometer (ACC) Noise

The accelerometers possess biases and scale factors which are unknown, but can estimated in the system. Additionally, they have one less sensitive axis, however according to Kim, its chosen orientation in the cross-track direction has no effect on the SST measurements and this fact can be neglected. The random noise signal in the accelerometer measurements has a power spectrum which is inversely proportional to its frequency, or $\frac{1}{f}$, which is known as pink noise.

3.4.2 GPS Noise

Gaussian random noise is added to the range calculated from the GPS carrier phase, with a standard deviation (σ) of 3mm.

3.4.3 KBR Noise

This is the noise added to the SST observations perfectly calculated from the measurement model equations. It is the most complex of the noise models as it contains the error contributions of six different sources. The SST noise generation is done as follows:

3.4.3.1 Oscillator Noise

The clocks on the two satellites use ultra-stable oscillators (USO) to keep accurate time. However, even these highly accurate oscillators are not without imperfection and there does exist a level of drift in them. While a

large component of this error is offset due to the mirrored positions of the spacecrafts, an effect does remain. Any time-keeping errors manifest in the frequencies of KBR transmissions, and by extension the phase calculations and thus the range. Kim [5] describes the detailed process by which the Allan variance of the clocks is converted to frequency noise, integrated to phase noise, then converted to noise in the range measurements through a specified transfer function.

3.4.3.2 Cone Error

Another source of range error comes from the fact that the attitude control system is not able to maintain perfect LOS alignment of the bore-sights onboard the two satellites, and therefore radio transmission/reception is not done perfectly along the true LOS. This off-pointing presents a phase error which has a proportional relationship to the cone angle, or the angle by which the satellite is offset from pointing along the LOS.

3.4.3.3 Multipath Noise

An indirect effect of the cone error is that some of the radio signal does not hit the phase center of the antenna, but reflects off other surfaces such as the K-band horn. This indirect signal is known as multipath error.

3.4.3.4 System Noise

In order to account for random errors that cannot be modeled in any other fashion, Gaussian white noise is added to the measurements.

The previous four error contributions are summed into a single signal, then naively differentiated via forward differencing, transforming the noise from range noise to range-rate noise. Then, one additional error type is added, which affects the range-rate, but not the range.

3.4.3.5 Thermal Noise

The effect of thermal distortion on the instruments and signal are not well modeled, however files containing a time-series of CBE thermal noise are provided by JPL [31].

This thermal noise is added to the rest of the errors, and a second differentiation is performed, arriving at the total noise contribution to the range-acceleration measurements.

3.4.4 Star Camera (SCA) Noise

Finally, the star cameras, which provide observations in order to control the yaw, pitch, and roll have random errors added to the measurements along all three axes.

3.4.5 Comparison with Real Flight Data Residuals

With access to actual GRACE flight data, as well as gravity field solutions from those data, a metric for assessing simulation validity is available. In this section, the term "real range-accelerations" refers to those derived by applying the standard 100mHz CRN-filter (defined in Chapter 4) to actual mission KBR data and their resulting post-fit residuals from the solution algorithm. By comparing both the residuals in the time domain for real versus simulated data, as well as the PSD of the real residuals vs. the PSD of the simulated noise, an idea of how well the setup is emulating reality can be obtained. Figures 3.9 and 3.10 show such a comparison.

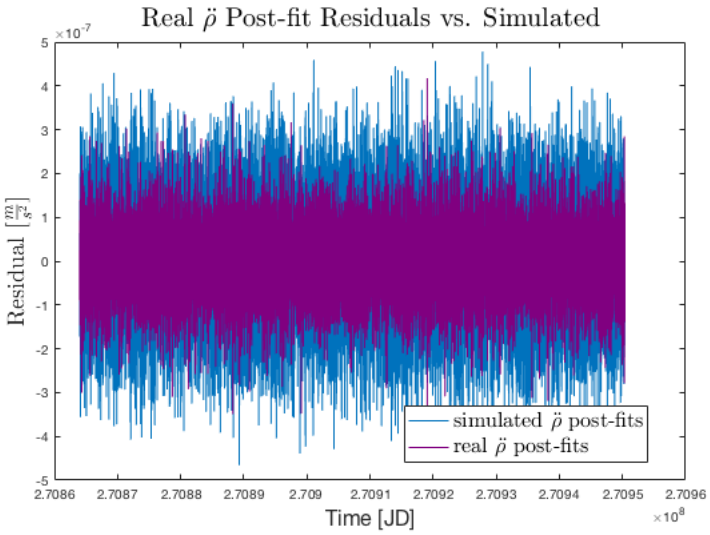

Figure 3.9: Real range-acceleration residuals vs. simulated

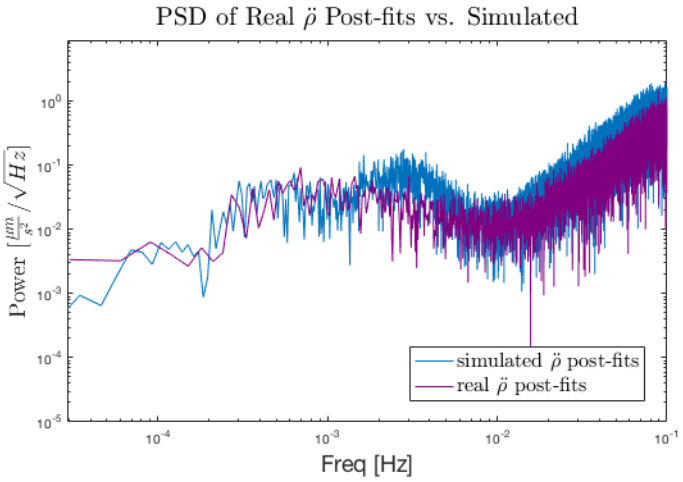

Figure 3.10: PSD of real vs. simulated residuals

When adding the noise models to the simulation, the time domain and power spectrum for both the real and simulated post-fit residuals are very comparable, both being dominated at high-frequencies by noise. While not a perfect match, this is an indication that the simulations are approximating reality reasonably well. Figure 3.11 shows the PSD of the noise signal itself, and the pre-fit residuals from simulations with and without that noise. In both cases, the simulated pre-fits display the familiar 1-cpr signal, reflecting actual gravity signal due to mean field difference between the simulation and the fit orbits. Their height above the noise signal at the low end is indicative of very good SNR, which rapidly degrades past a certain frequency threshold. The simulated noise is behaving as desired, avoiding adding much power to the frequency band that contains the gravity signal and contributes most of the power present above that frequency, if not all. It has the expected curve of

violet noise, or twice differentiated white noise, which is proportional to ω^4, where $\omega = 2\pi f$.

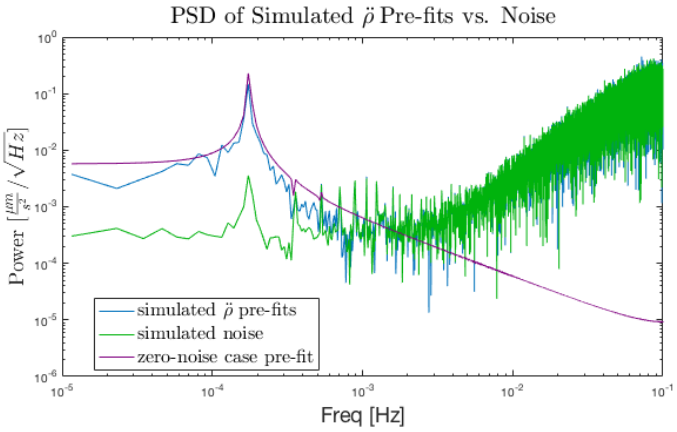

Figure 3.11: PSD of simulated pre-fits vs. noise

It should be noted as a reminder here that just because the simulation is approximating reality well, it does not mean the range-accelerations are providing "good" solutions. The DDV/DEV triangle plots for this simulation are provided in Figure 3.12, and they clearly show very high errors, particularly at higher degrees, indicating these degree and order estimates are quite far from the truth.

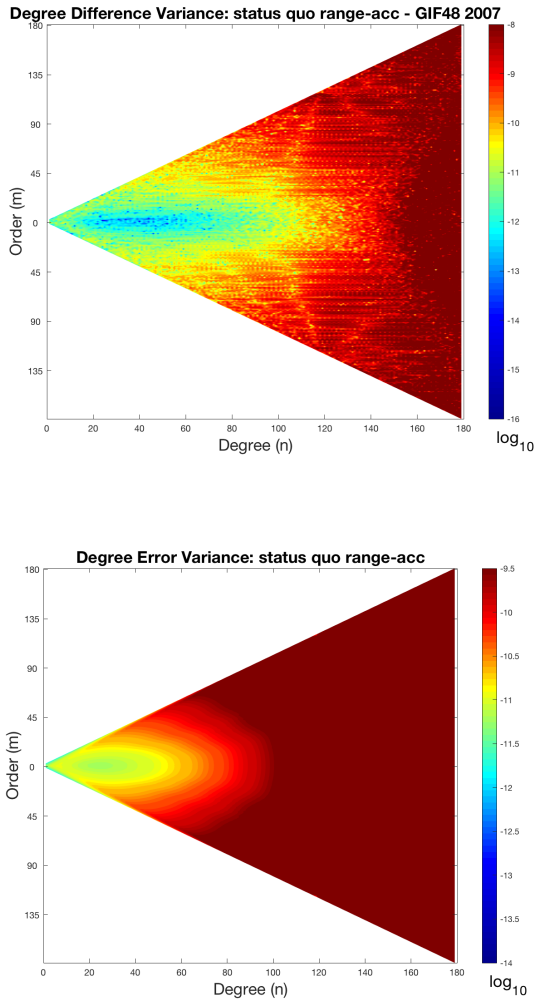

Figure 3.12: DDV/DEV triangle plots for the status quo range-acc solution

When compared to the triangle plots of the baseline in Figure 2.3, it is clear that this solution's errors climb higher much more rapidly. There are almost no "low" errors present in the DEV at all, and even the low-degree errors in the DDV are much greater than the baseline solution. The errors at higher orders are significant even below degree-60.

3.5 Error Sensitivity

With confirmation that the formulation of the range-acceleration simulation procedure is not causing the large degradation in the gravity field estimate, an analysis of the sensitivity of the solution to each of the four main noise sources can progress. The following figures compare the status quo range-acceleration solution to several variations, each one removing one source of error in order to ascertain which source is contributing most to the problematic results. The reference solution, indicated by the black line, is the GIF48 truth field. The more a noise source contributes to the gravity field errors, the more closely the solution coefficients should match the reference when excluding it.

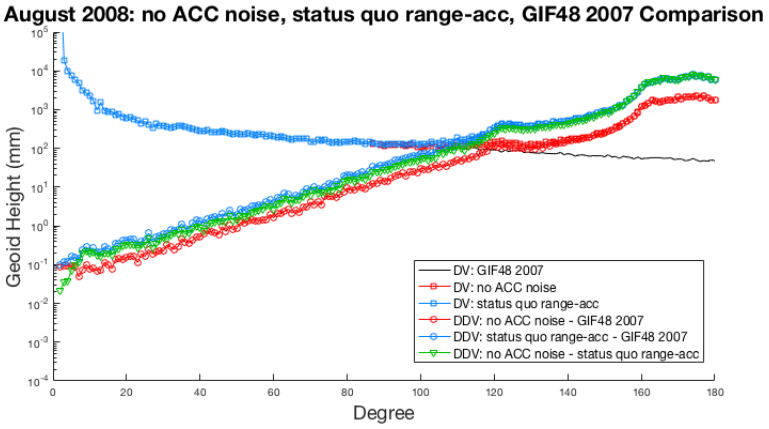

Figure 3.13: No ACC noise vs. status quo range-acc

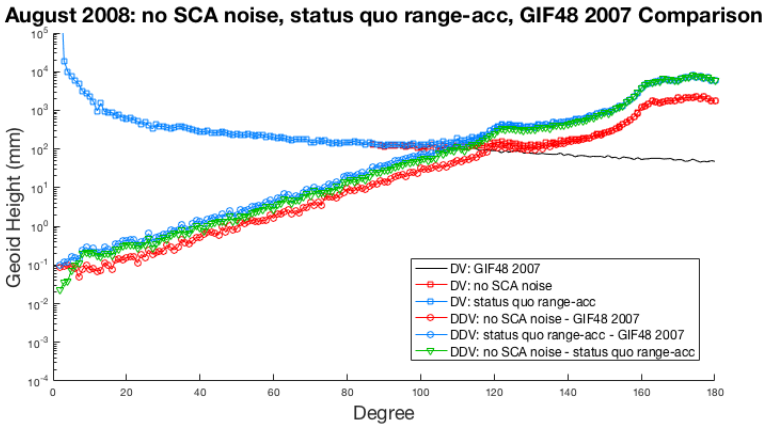

Figure 3.14: No SCA noise vs. status quo range-acc

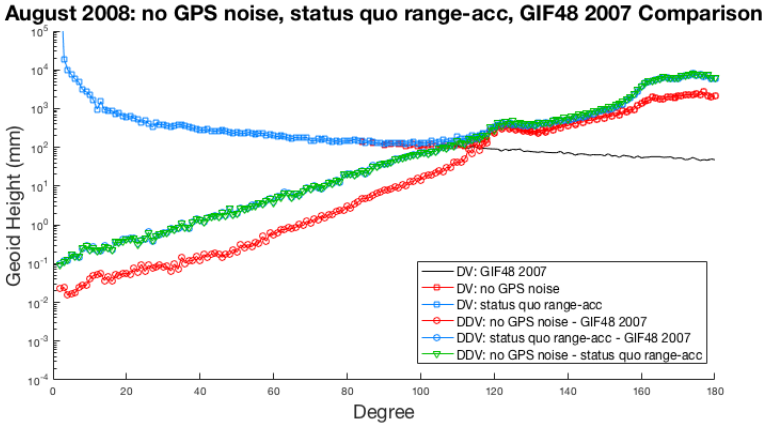

Figure 3.15: No GPS noise vs. status quo range-acc

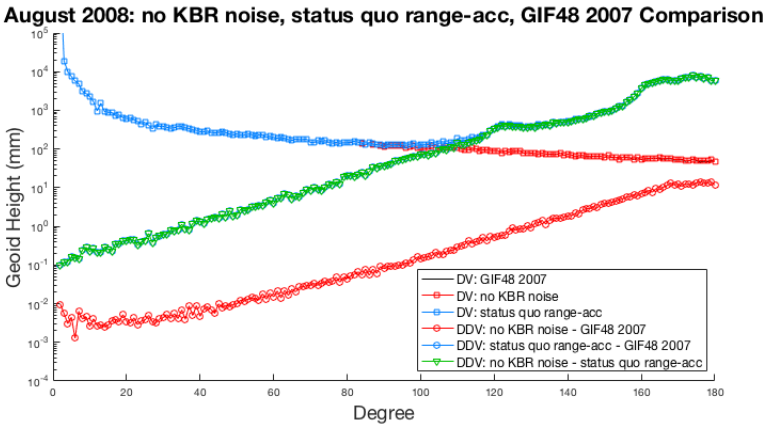

Figure 3.16: No KBR noise vs. status quo range-acc

These comparisons make it very obvious that the main contributor to the large errors in the status quo range-acceleration gravity field estimate are due to the KBR noise. Removal of the ACC, GPS, and SCA noise sources also improved the solutions, however less dramatically and uniformly than removal of the KBR noise. Interestingly, removal of the ACC noise yielded an almost identical solution to one with the SCA noise set to zero, as seen in Figure 3.17. This suggests that the SCA noise mainly contributes through errors in rotation of the ACC data. Additionally, removal of the GPS errors made notable improvement in the solution at the lower harmonics, while the ACC/SCA removal most benefitted degrees in the 120-160 range, shown in Figure 3.18.

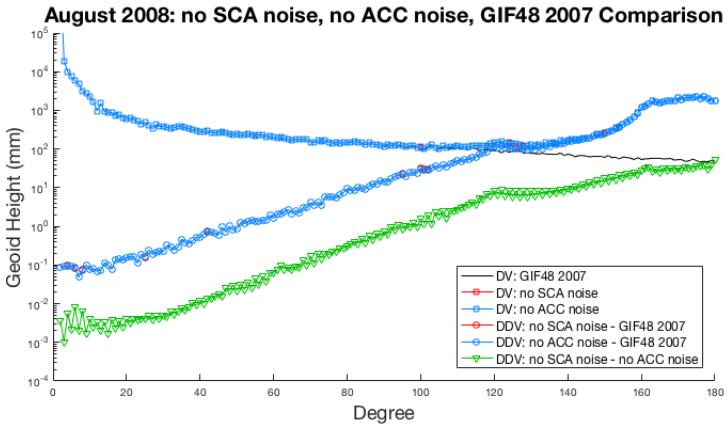

Figure 3.17: No SCA noise vs. no ACC noise

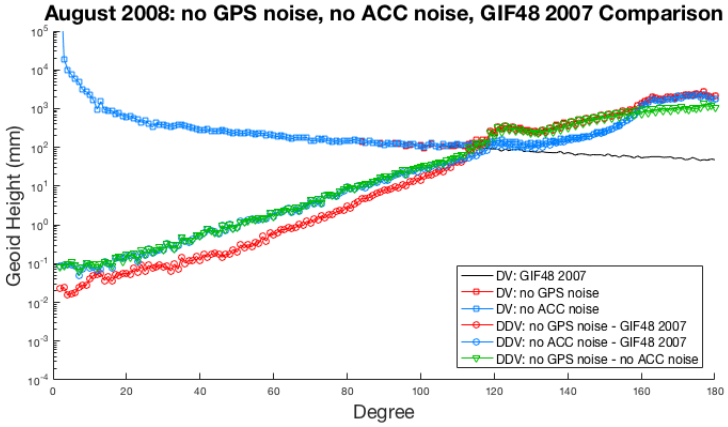

Figure 3.18: No GPS noise vs. no ACC noise

3.6 Observability

The poor quality of the status quo estimate begs a question of observability in the linear system. The connection between the range-acceleration model and the null space (if any) of the mapping matrix, $\boldsymbol{H}$, needs to be examined to determine if any parameters of the system are unobservable. This can be accomplished through singular value decomposition (SVD). A more detailed explanation of this analysis is provided by McCullough [15], however the basic steps are as follows. The $\boldsymbol{H}$ matrix can be decomposed into a diagonal matrix of singular values, $\boldsymbol{\Sigma}$, and left/right singular vectors, $\boldsymbol{U}/\boldsymbol{V}$, as in Equation 3.14.

$$\boldsymbol{H} = \boldsymbol{U}\boldsymbol{\Sigma}\boldsymbol{V}^T \tag{3.14}$$

The formulation of the GRACE inverse problem is known to be an ill-posed system, as opposed to a rank-deficient one, therefore none of the singular values are identically zero. However, some singular values do drop off in magnitude and are much closer to zero, making the linear combination of parameters which correspond to those lower values "nearly unobservable", or at least more unobservable than the rest. A plot of the singular values for the KBR data only is provided in Figure 3.19.

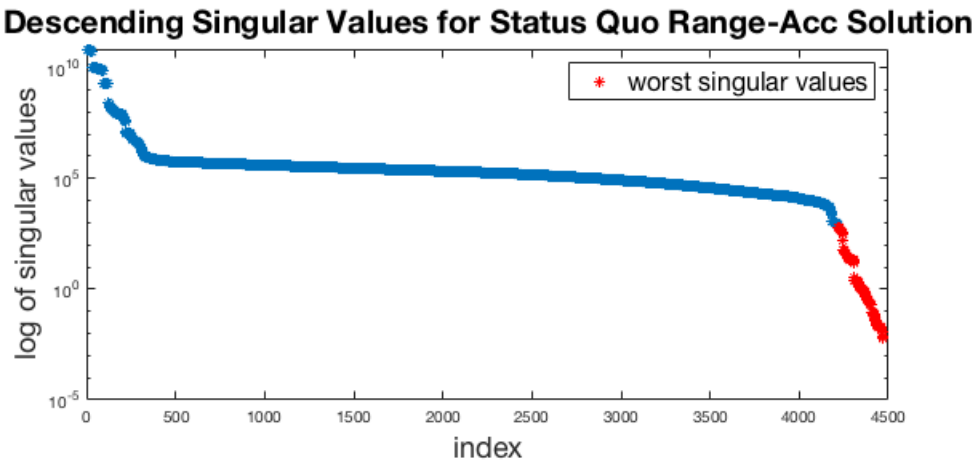

Figure 3.19: Log plot of singular values

In [15], the orthonormality of $\boldsymbol{V}$ is taken advantage of in order to determine which parameters contribute to those lower values most. The RMS sum of the rows of $\boldsymbol{V}$ corresponding to the lowest singular values are computed, and the nearer the sum is to 1, the greater the corresponding parameter contributes to the ill-conditioning of the system. In that study it was found that the largest contributing parameters were the initial positions of the satellites for each arc, which are extremely correlated, the accelerometer scale factors, and the initial velocities. The gravity field coefficients were not a significant contributor to the ill-conditioning. Figure 3.20 shows the results of the same analysis for the range-acceleration formulation. The first 750 parameters being estimated, which include only the the daily initial positions, velocities, and scale factors, have several rms values at or very near 1. The gravity coefficients begin at parameter 751, beyond which none of the RMS values exceed 0.02.

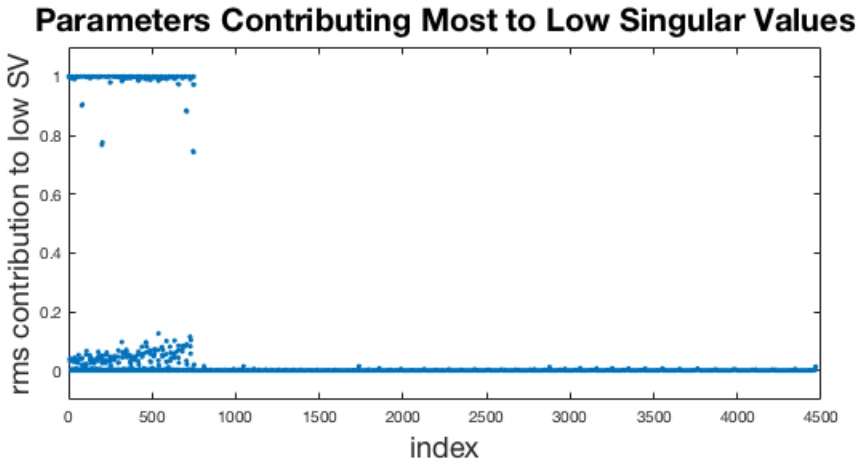

Figure 3.20: Worst contributing parameters

This indicates that the gravity field itself is no less observable when attempting estimation via range-accelerations. That is, there is no conceptual limitation preventing proper estimation of the gravity field using the range-acceleration measurements. These results, however, do reflect their high sensitivity to noise, particularly KBR noise, which has increased power at higher frequencies due to the second differentiation. The next chapter details this, as well as how the range-acceleration measurements themselves are obtained, and the results of various attempts to reduce the noise in the observations are presented.

Chapter 4

Differentiation of the Phase-Derived Range Observations

The fundamental measurement obtained from the GRACE satellites is phase offset information, at a rate of 10Hz. These phase observables are converted into biased range, then compressed, corrected, and differentiated to obtain the time derivative measurements [19]. The KBR Level-1B (L1B) data product provided by NASA's Jet Propulsion Laboratory contains these values for the range (biased), range-rate and range-acceleration pseudo-observations, as well as their respective light-time and antenna offset corrections. These time series are created by applying a finite impulse response (FIR) filter, as well as its first and second time derivatives, to the dual one-way phase measurements. The act of differentiation acts as a high-pass filter, amplifying the noise level at high frequencies and degrading the signal-to-noise ratio (SNR). As seen in the previous chapter, in the case of range-accelerations this gain in high-frequency noise drowns out the gravity signal. The SNR is simply too low, and allows the noise to overwhelm the estimation algorithm, making it impossible to recover a viable estimate of the gravity field. This chapter attempts to fine-tune the CRN-filter, as it is known, which is typically used to obtain the measurement derivatives, as well as analyzes solutions produced via an alternative method of obtaining range-accelerations.

4.1 Range Observable Overview

The GRACE microwave ranging system broadcasts over two different frequencies in order to be able to correct for ionospheric delay, which is frequency dependent. These two frequencies are 24GHz and 32GHz, falling into the K and Ka-bands respectively. A schematic of the ranging system is provided in Figure 4.1.

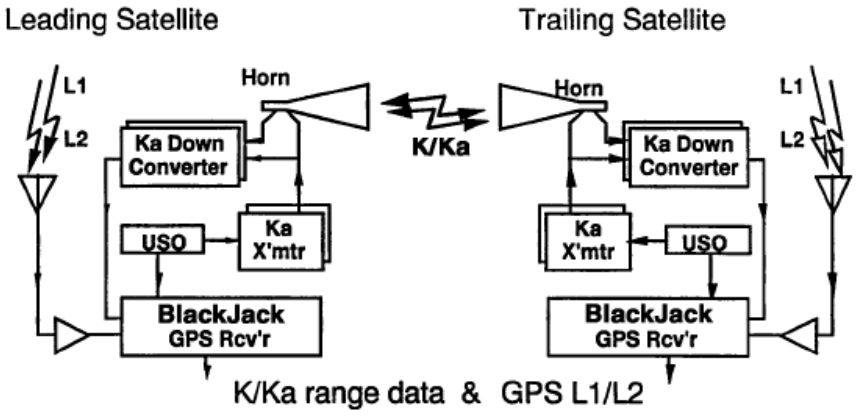

Figure 4.1: Schematic of the microwave ranging system [5]

The phase offset of the signal, measured at the receiving satellite in fractions of cycles, is directly related to the distance travelled by the incoming wave. The conversion from phase measurement to biased range is expressed in Equation 4.1.

$$\mathbf{\Psi}_{K/Ka} = c \cdot \frac{(\psi_{A_{K/Ka}} + \psi_{B_{K/Ka}})}{(f_{A_{K/Ka}} + f_{B_{K/Ka}})} \tag{4.1}$$

where,

$\mathbf{\Psi}_{K/Ka}$ = K or Ka biased range,

c = speed of light,

$\psi_{A_{K/Ka}}$ = K or Ka phase measurement at satellite A,

$\psi_{B_{K/Ka}}$ = K or Ka phase measurement at satellite B,

$f_{A_{K/Ka}}$ = K or Ka frequency of satellite A,

$f_{B_{K/Ka}}$ = K or Ka frequency of satellite B.

Additionally, the ionosphere-free biased range is calculated as,

$$\text{biased range} = (\text{ion}_{Ka} \cdot \Psi_{Ka}) - (\text{ion}_{K} \cdot \Psi_{K}) \tag{4.2}$$

where,

$$\text{ion}_{Ka} = 16/7,$$
$$\text{ion}_{K} = 9/7.$$

And finally, the biased range is corrected based on the time-of-flight (TOF) of the radio signal and the offset of the antenna phase center from the center of mass of the satellite. This adjusted quantity is known as the dual one-way range (DOWR).

$$\text{DOWR} = \text{biased range} + \text{lighttime correction} + \text{antenna offset} \tag{4.3}$$

This 10Hz data is differentiated by the filter described in the next section and compressed to 5-second observations. Since the issue with range-acceleration

seemingly lies in the fact that the measurements themselves, arrived at by digital filtering, are simply too noisy to be useful in estimating the gravity field, a sensible candidate for reduction of the noise introduced into the observations is the tuning of the filter itself.

4.2 The CRN-filter

There exists a multitude of options for calculating the time derivative of a signal, and usually the optimal choice is extremely domain-specific. In the application of processing GRACE data, the filter is tasked to simultaneously low-pass filter, compress, and differentiate the input signal. Thomas [6], lays out in detail the benefits of taking a "frequency first" approach when designing the method for computing the derivatives of the range observations. Since the gravity signal has known spectral properties which need to be preserved in the output, it is desirable to design a filter which has its mainlobe almost entirely in the passband of interest (0.01mHz to ∼100mHz), with as little sidelobe ripple as possible. For computational and intuitive simplicity, the filter is first constructed in the frequency domain, then Fourier transformed into the time domain. The time domain filter needs to have a finite window, a requirement which is achieved through a class of window functions formed by Convolving a Rectangular time-domain window with itself N_c times. This gives the CRN-class of digital filters a simple expression in the frequency domain, which is easily tunable to generate signals with the spectral properties desired. The following equations describe the computation of the weighting functions used

in the CRN-filter and the default parameter values currently used in the calculation of the compressed range and its derivative products.

The parameters, the knobs which can be tuned to control the filter, are given with their default values and defined as follows:

$$
\begin{aligned}
f_s &= \text{raw data rate} && = 10Hz, \\
N_c &= \text{number of self-convolutions (odd)} && = 7, \\
T_f &= \text{time window} && = 70.7s, \\
B &= \text{target low-pass bandwidth} && = 0.1Hz, \\
f_0 &= \text{J2 frequency} && = 0.37 \times 10^{-3}Hz, \\
N_B &= \text{number of bins in the passband} && = B \cdot T_f, \\
N_f &= \text{number of raw data points in the window} && = f_s \cdot T_f.
\end{aligned}
$$

These variables are used to calculate the output 0.2Hz KBR data according to the following equations.

$$\rho_i^{out} = \sum_{n=-N_h}^{N_h} F_n \cdot \rho_{i-n}^{raw} \tag{4.4}$$

where $N_h = \frac{(N_f-1)}{2}$ and the weighting function, F_n, and its components are given as,

$$F_n = \frac{1}{F^{Norm}} \sum_{k=-N_h}^{N_h} H_k \cdot \cos\left(\frac{2\pi kn}{N_f}\right), \text{ for } |n| \leq N_h \tag{4.5}$$

$$H_k = \sum_{m=-N_B}^{N_B} \left(\frac{\sin[\pi(k-m)/N_c]}{\sin[\pi(k-m)/N_f]}\right)^{N_c} \tag{4.6}$$

$$F^{Norm} = \sum_{n=-N_h}^{N_h} \left[\cos\left(\frac{2\pi f_0 n}{f_s}\right) \cdot \sum_{k=-N_h}^{N_h} H_k \cdot \cos\left(\frac{2\pi kn}{N_f}\right)\right] \tag{4.7}$$

The first and second time derivatives are computed similarly, with the time derivatives of the F_n weighting function replacing it.

$$\dot{\rho}_i^{out} = \sum_{n=-N_h}^{N_h} \dot{F}_n \cdot \rho_{i-n}^{raw} \quad ; \qquad \dot{F}_n = \frac{1}{F^{Norm}} \sum_{k=-N_h}^{N_h} -\left(\frac{2\pi k}{T_f}\right) \cdot H_k \cdot \sin\left(\frac{2\pi kn}{N_f}\right) \tag{4.8}$$

$$\ddot{\rho}_i^{out} = \sum_{n=-N_h}^{N_h} \ddot{F}_n \cdot \rho_{i-n}^{raw} \quad ; \qquad \ddot{F}_n = \frac{1}{F^{Norm}} \sum_{k=-N_h}^{N_h} -\left(\frac{2\pi k}{T_f}\right)^2 \cdot H_k \cdot \cos\left(\frac{2\pi kn}{N_f}\right) \tag{4.9}$$

The following three sections compare solutions produced by adjusting the three tunable parameters for the CRN-filter: B, N_c, and T_f.

4.2.1 Varying Bandwidth

By default, the GRACE data is processed with the filter setup with a nominal passband of 100mHz. As determined previously, the maximum frequency of interest, even when computing solutions up to d/o 180, lies around ∼34mHz. While this extra bandwidth serves as margin for the filter, ensuring that actual gravity signal is not removed, it also allows the high-frequency

noise to remain present in the signal as well. The solutions presented in this section compare the status-quo (100mHz) range-acc solution to ones with the bandwidth of the filter progressively dropped by 20mHz, from the default 100mHz for the baseline down to 20mHz.

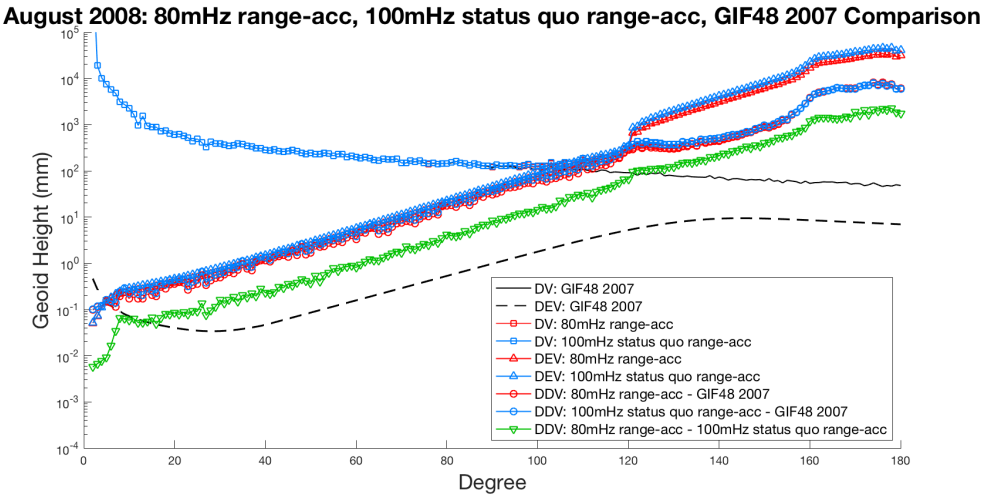

Figure 4.2: Reduced filter bandwidth, 80mHz

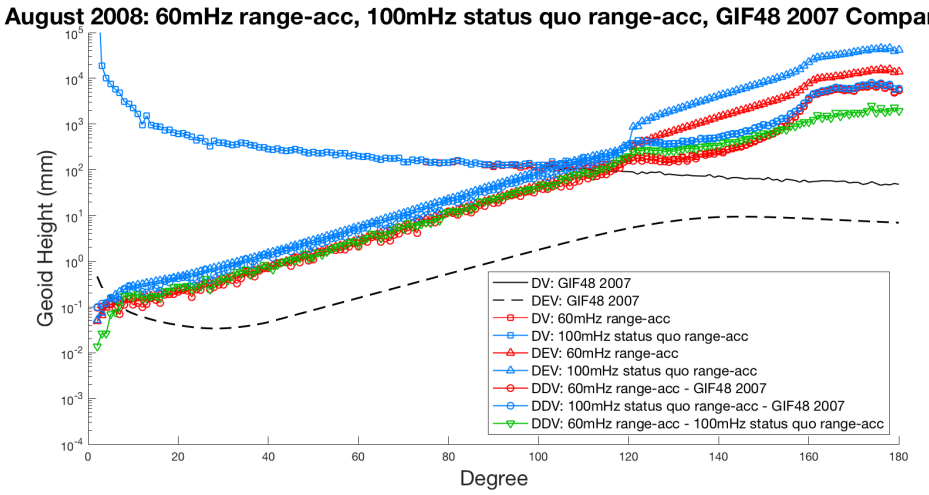

Figure 4.3: Reduced filter bandwidth, 60mHz

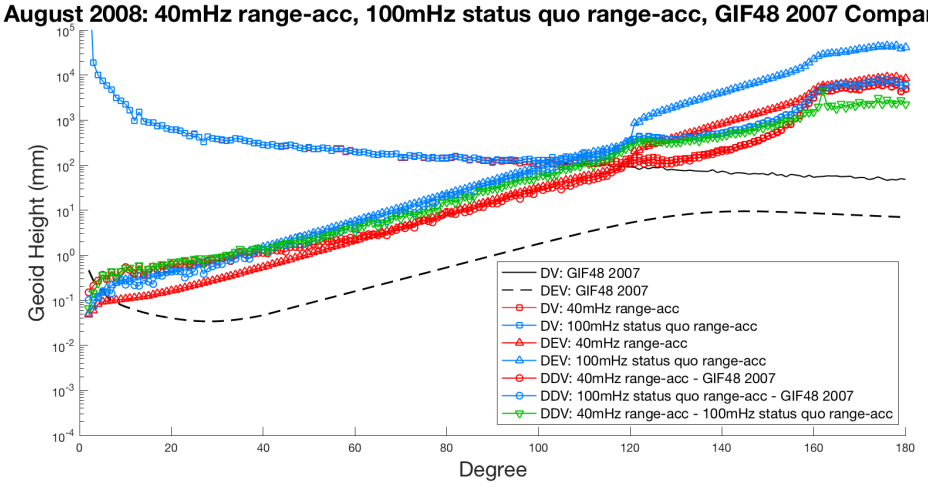

Figure 4.4: Reduced filter bandwidth, 40mHz

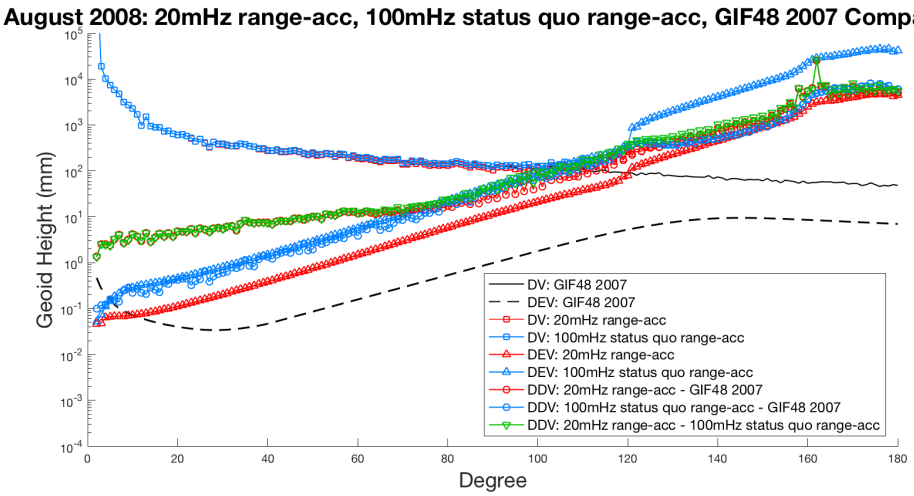

Figure 4.5: Reduced filter bandwidth, 20mHz

Several of the solutions improve over the 100mHz default solution, but only up to a point. In the sequence of Figures 4.2-4.5, the blue markers always denote the 100mHz status-quo solution, with red being the variation. When the red DDV appears below blue, the solution is improved over the status quo. The improvements continue until 40mHz, where the low degree DDV begins to creep higher than the 100mHz solution. However, this 40mHz passband solution produces the smallest high-degree deviations from the reference values and post-fit PSD. From there, the passband of the filter is dropped to 20mHz, below the bandwidth needed to allow the gravity signal of interest ($\sim$34mHz) to remain in the signal. As expected, once below that threshold, the quality of the solution is significantly diminished. Figure 4.6 compares the PSD of the post-fit residuals from these experiments, while Figure 4.7 compares the PSD of the pre-fits.

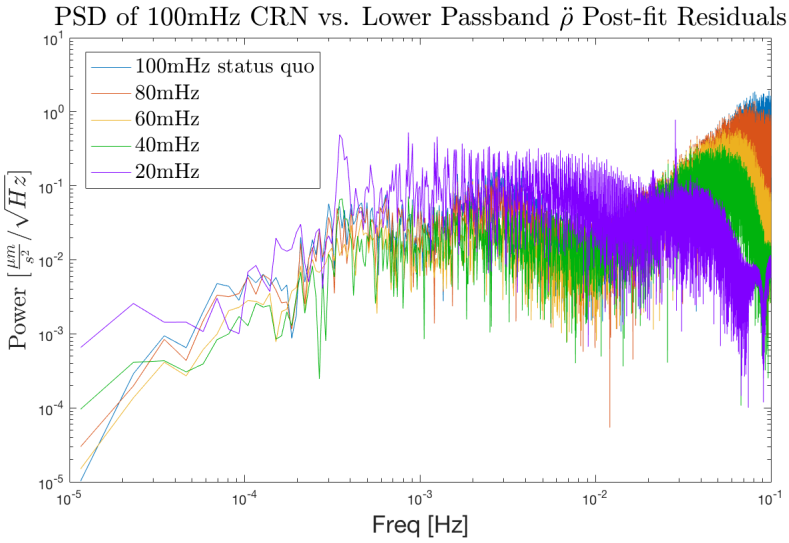

Figure 4.6: Reduced filter bandwidth post-fit residuals

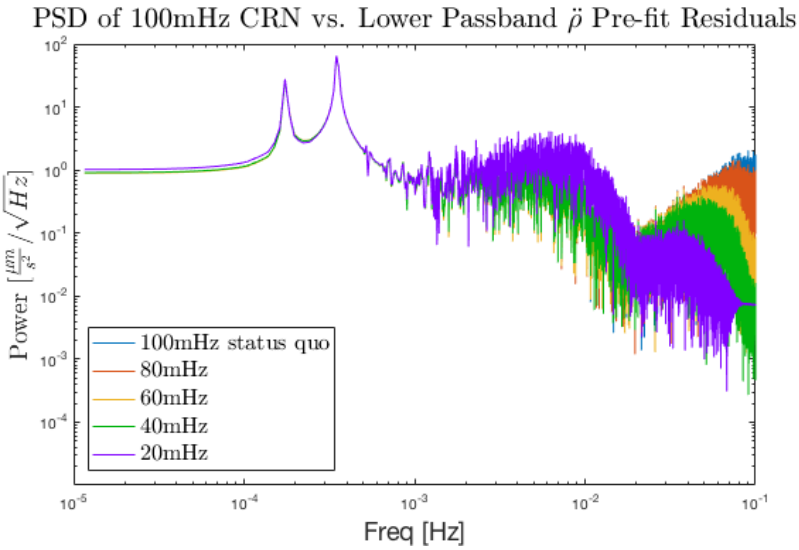

Figure 4.7: Reduced filter bandwidth pre-fit residuals

From these plots, it is evident at the high end of the spectrum that the reduction of the passband is performing as expected. The power of the signal at high frequencies does in fact reduce as the width of the passband shrinks. There is a balance that must be achieved for the ideal passband cutoff, as too high (100mHz) allows too much noise to corrupt the solution, while below 40mHz is where the errors grow larger yet again. In terms of bandwidth, it seems the tuning best suited for range-accelerations lies somewhere in the 40-60mHz range. Since 40mHz produces the best PSD and gravity field solution at the highest degrees, it will be used in the comparisons in the next chapter.

4.2.2 Number of Self-Convolutions

According to Thomas [6], the number of self-convolutions in the CRN-filter controls the rate at which magnitude of the sidelobes of the signal drops off, decreasing as N_c increases. This is a benefit of the filter, as it would be optimal for the magnitude of the sidelobes to drop to zero immediately outside the passband. However, this does come with a drawback, as the width of the basis rectangle decreases inversely proportionally with N_c, meaning that the width of the main lobe and spacing of the sidelobes increases. This means that the skirt width of the signal broadens further past the low-pass cutoff frequency. While some degree of this is acceptable in GRACE processing, N_c must be balanced correctly with window length to yield good results at the higher required frequencies. The following figures compare solutions at $N_c = 5, 9, 11,$ and 13 with the default $N_c = 7$ solution.

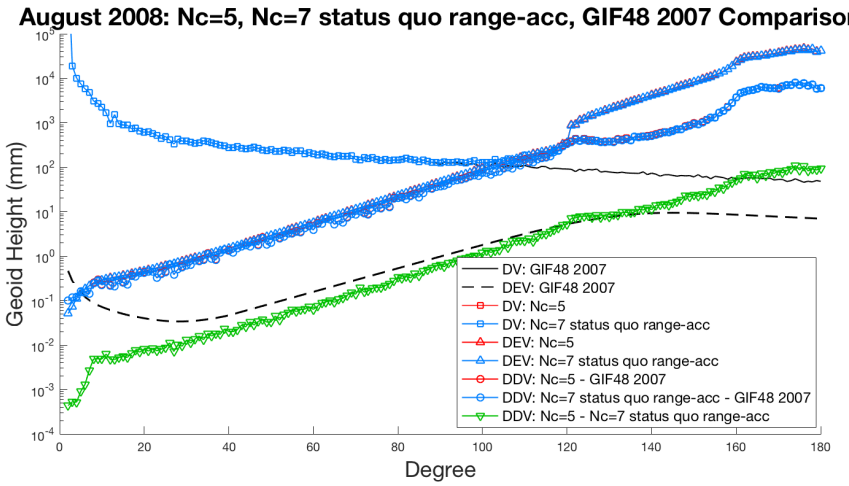

Figure 4.8: Varied convolutions, $N_c = 5, 7$

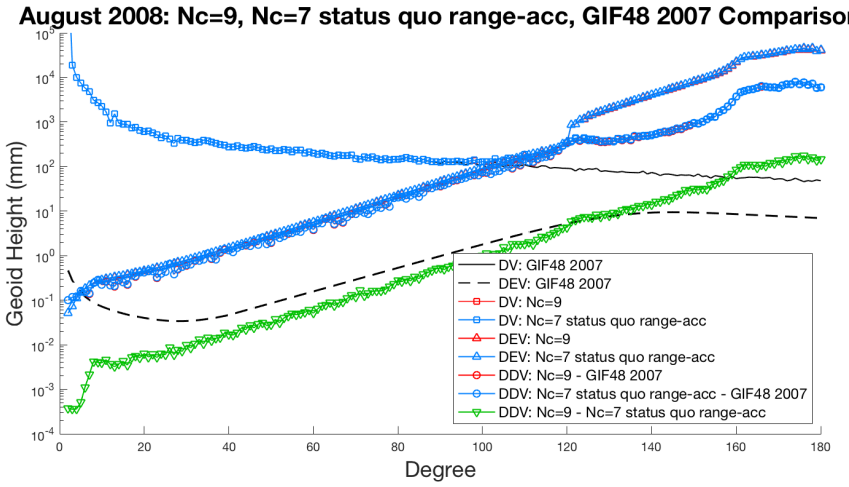

Figure 4.9: Varied convolutions, $N_c = 9, 7$

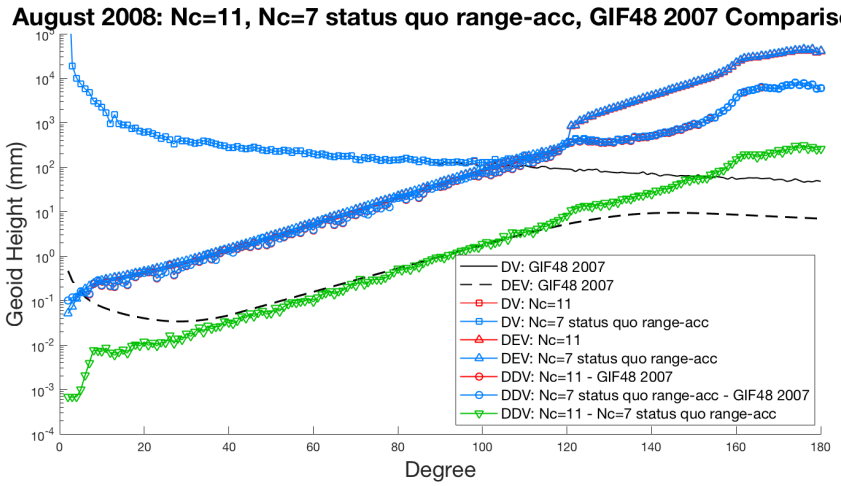

Figure 4.10: Varied convolutions, $N_c = 11, 7$

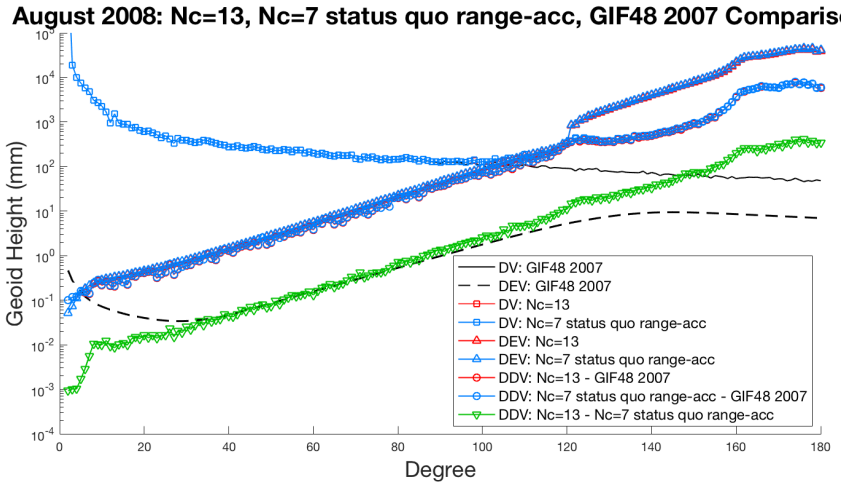

Figure 4.11: Varied convolutions, $N_c = 13, 7$

All solutions obtained from varying the number of convolutions lie right on top of one another, indicating that tuning the N_c parameter alone has little to no effect on the range-acceleration based solutions.

4.2.3 Varying Time Domain Window Length

The only remaining CRN-filter parameter available for tuning is the length of the time domain window, which refers to the number of seconds around the observation of interest which are used to compute the rate of change of the signal. The longer the time window, the more correlated the errors in the output signal will be, having the possibility of affecting the resulting gravity field solution when changed. The following figures compare solutions which both shorten and lengthen the filter time window, comparing the default $T_f = 70.7s$ to windows of length $T_f = 30.7s,\ 50.7s,\ 90.7s,$ and $110.7s$.

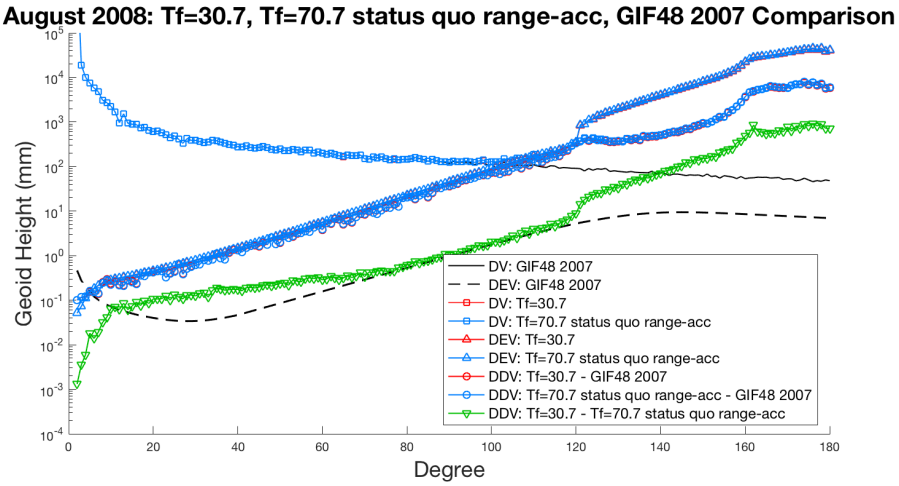

Figure 4.12: Varied time window, $T_f = 30.7, 70.7$

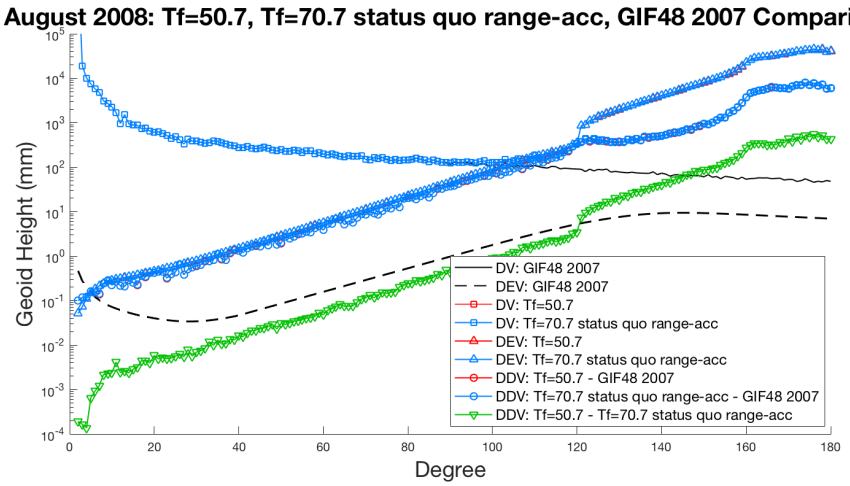

Figure 4.13: Varied time window, $T_f = 50.7, 70.7$

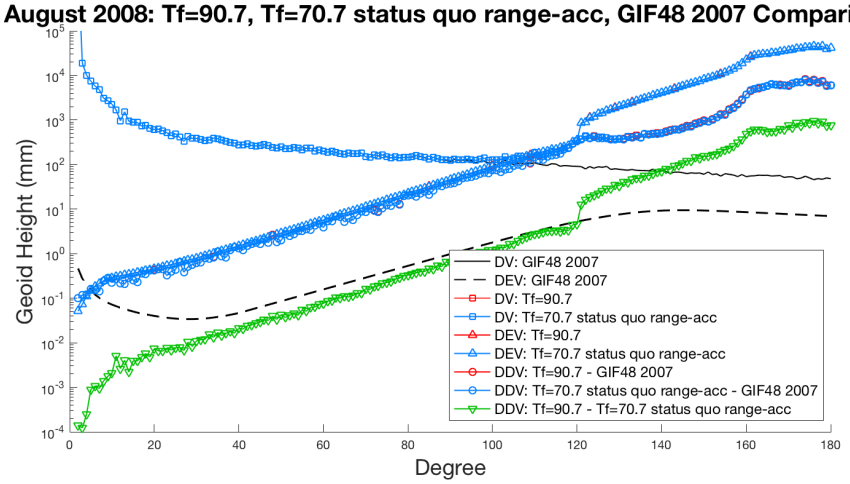

Figure 4.14: Varied time window, $T_f = 90.7, 70.7$

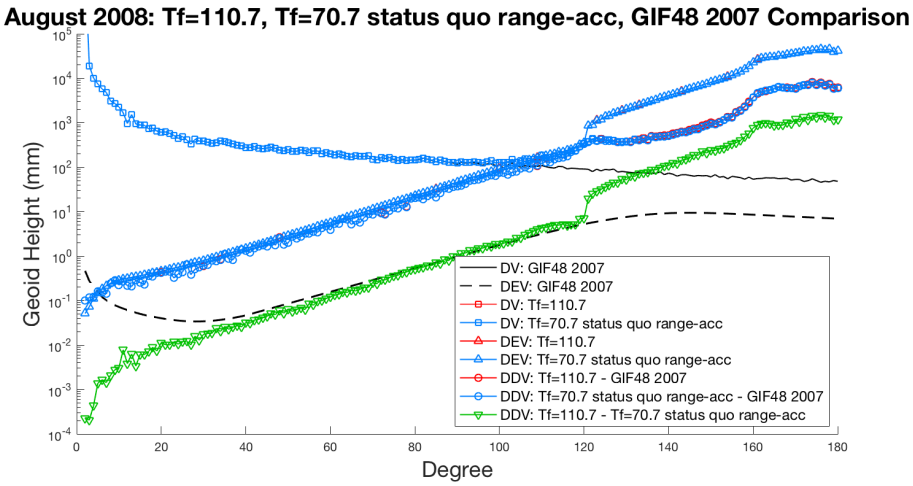

Figure 4.15: Varied time window, $T_f = 110.7, 70.7$

Again, the solutions are virtually identical. With each of the tunable parameters for the CRN-filter having been adjusted in this section, the only observed improvement in the gravity field came by adjustment of the passband. This indicates the default 100mHz setting is not perfectly tuned for the application of processing GRACE data into filtered range-accelerations. Gravity field estimates utilizing range-accelerations clearly benefit by adjusting the CRN-filter to 40-60mHz. In the next section, a different method of obtaining the time derivative of the range observations altogether is investigated in an effort to reduce the noise present in the range-acceleration measurements, and improve gravity estimates based on them.

4.3 Smooth, Noise-Robust Differentiation

By design, the CRN filter utilized to derive the L1B 5-second range, range-rate, and range-accelerations from the 10-HZ phase measurements made by the KBR system is a smoothing differentiator, but was not derived explicitly to suppress the high-frequency noise present in the differentiated signals. This choice was made to retain as much of the gravity signal as possible in the data, allowing the end-user to perform filtering and noise suppression to suit their specific needs should they so choose. As mentioned, the differentiation process amplifies the noise present in the signal at high frequencies, degrading the SNR, and in turn, the gravity field solution due to the high sensitivities involved. With expected accelerations due to mass anomalies on the Earth to be on the order of $30\frac{nm}{s^2}$, leaving the high-frequency noise in the range-accelerations unmitigated easily eclipses the gravity signal in magnitude, resulting in solutions for the gravity field which are poorer in quality by an order of magnitude or more. With the goal of achieving differentiated range-accelerations which are as accurate and contain as little noise as possible, another method of computing them is explored here. Examination of the literature uncovered a filtering process which is meant to calculate highly accurate first and second derivatives while specifically suppressing high-frequency noise in the time series. The designer, Holoborodko [13], refers to it as "smooth, noise-robust (NR) differentiation", and it was employed by Tregoning [7] to achieve an impressive mascon gravity field solution with the resultant range-accelerations. This makes the

filter a worthy candidate for achieving feasible gravity field solutions represented in spherical harmonics using variational methods. The derivation and design of the filter is outlined in [13] and described as follows.

4.3.1 Derivation of the Filter

Although widely used in numerical applications, standard N-point central difference stencils for computing derivatives possess no high-frequency noise suppression properties. A more desirable filter can be constructed if it is required it to achieve precision on low frequencies and suppression of noise at high frequencies (noise-robust). The type of filter to be designed should pass as much low-frequency signal as possible, while removing information above a certain cutoff frequency which is thought to contain only noise. This type of filter is known as a maximally flat, low-pass differentiator. The ideal differentiator has certain properties which achieve these goals , and can be used to derive the conditions for a digital filter to use in the GRACE application. These properties are displayed in Equation 4.10.

$$H_d(e^{i\omega}) = \begin{cases} i\omega, & |\omega| \leq \omega_c \\ 0, & \omega_c \leq |\omega| \leq \pi \end{cases} \tag{4.10}$$

Here, $H_d(e^{i\omega})$ is the frequency response of the ideal differentiator, ω is the normalized angular frequency, and ω_c is the cutoff frequency. The general form of the N(odd)-point central difference numerical derivative at a point,

x^*, is given by Holoborodko [13] as

$$f'(x^*) \approx \frac{1}{h} \sum_{k=1}^{M} c_k \cdot (f_k - f_{-k}), \tag{4.11}$$

where $f_k = f(x_k),\ x_k = x^* + kh,\ k = -M, ..., M,$ and $M = \frac{N-1}{2}$. The step-size is denoted by h. The frequency response of the central difference filter is

$$H(e^{i\omega}) = 2i \cdot \sum_{k=1}^{M} c_k \cdot \sin(k\omega) \tag{4.12}$$

If a differentiator is desired which, in practice, behaves like the ideal one, Equation 4.11, along with certain conditions implied by 4.12, can be used to solve for the noise-robust filter coefficients, c_K. Within the some passband cutoff, ω_c, the frequency response of the filter should have high-order tangency with the ideal differentiator, beyond that it should tend to zero. These conditions are represented mathematically in Equation 4.13.

$$\begin{aligned} \left.\frac{\partial^i H(e^{i\omega})}{\partial \omega^i}\right|_0 &= \left.\frac{\partial^i H_d(e^{i\omega})}{\partial \omega^i}\right|_0 \quad i = 0, ..., n \\ \left.\frac{\partial^j H(e^{i\omega})}{\partial \omega^j}\right|_\pi &= 0 \qquad\qquad\quad j = 0, ..., m \end{aligned} \tag{4.13}$$

where n is the desired order of tangency, and $m = \frac{N-3}{2}$. The general solution for c_k contains binomial coefficients (the terms in parenthesis, representing "n choose k" notation) and is given by the expression in 4.14.

$$c_k = \frac{1}{2^{2m+1}} \left[\binom{2m}{m-k+1} - \binom{2m}{m-k-1} \right] \tag{4.14}$$

For any chosen filter length, N, and desired order of tangency, n, this derivation enables calculation of the coefficients of the robust filter. Holoborodko extends this filter to the second order with the following expression.

$$f''(x^*) \approx \frac{1}{2^{N-3} \cdot h^2} \left(s_0 \cdot f_0 + \sum_{k=1}^{M} s_k \cdot (f_k - f_{-k}) \right), \tag{4.15}$$

where s_k is generated according to the following recursive algorithm ($k = M...0$),

$$if\ k > M, s_k = 0;$$

$$if\ k = M, s_k = 1;$$

$$else,\ s_k = \frac{[(2N-10) \cdot s_{k+1} - (N+2k+3) \cdot s_{k+2}]}{(N-2k-1)}$$

It should be noted that these equations are specifically for central differences of regularly spaced data. Other derivations, for irregularly spaced data and forward or backward derivatives, are detailed in [13].

4.3.2 Solutions via the Noise-Robust Filter

The following figures compare range-acceleration solutions generated from the "smooth, noise-robust" filter against gravity field solutions from the default range-acceleration solution produced by the status quo range-accelerations. For the filter design, a second-order tangency is used, and the length of the filter varied from $N = 5$ to $N = 13$.

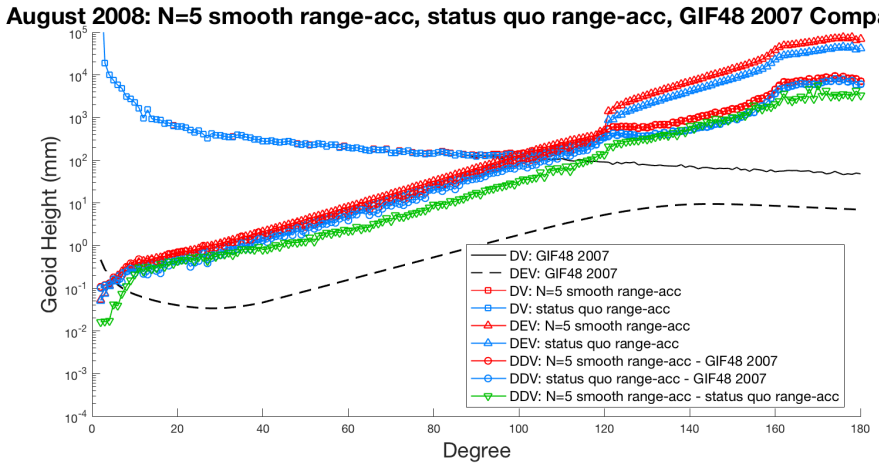

Figure 4.16: Noise-robust filter, N=5

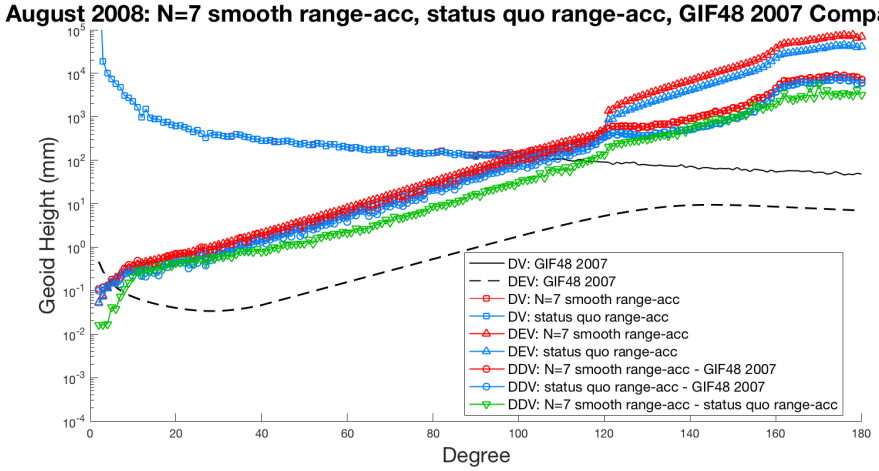

Figure 4.17: Noise-robust filter, N=7

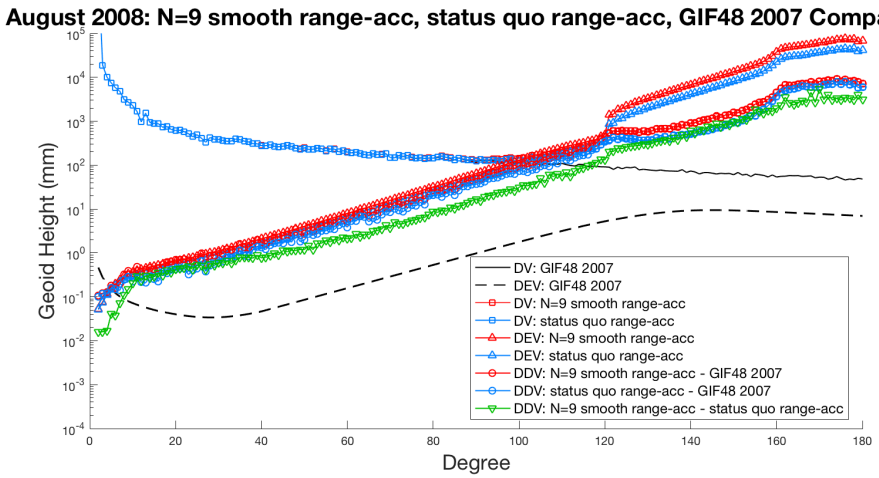

Figure 4.18: Noise-robust filter, N=9

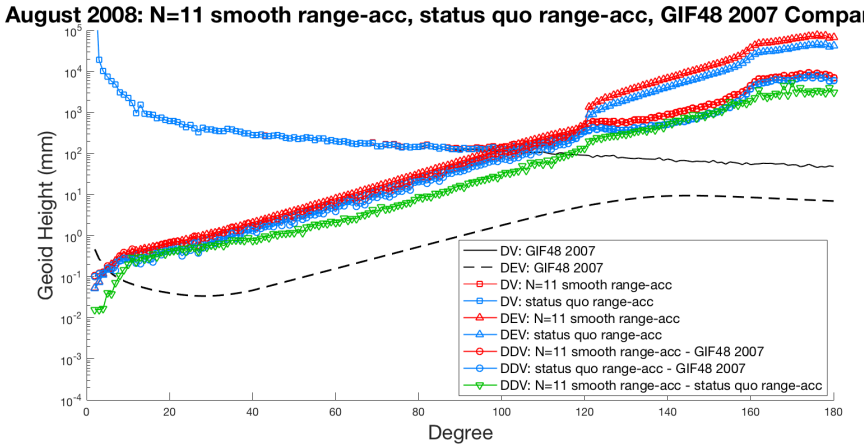

Figure 4.19: Noise-robust filter, N=11

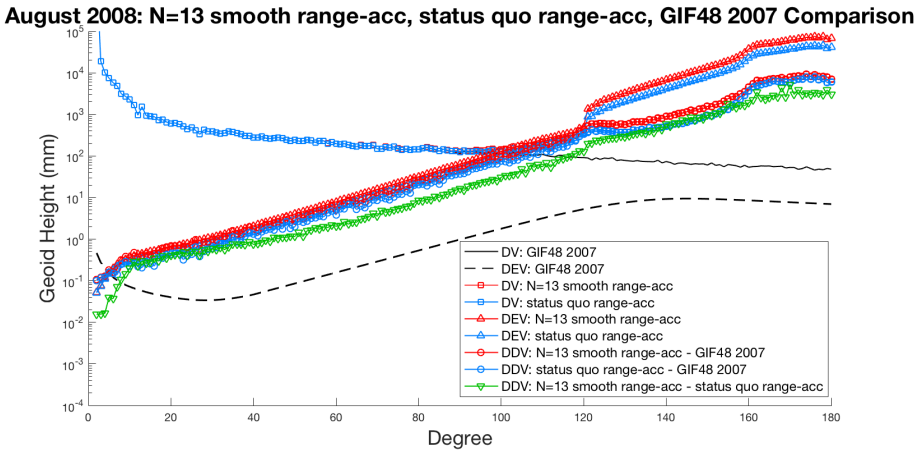

Figure 4.20: Noise-robust filter, N=13

Again, tuning of the filter provides no improvement in the results, and this alternative method of obtaining the time derivative of the range observations yields no tangible benefit. In fact, there is slight degradation from the already poor status quo solution.

4.4 Chapter Summary

Table 4.1 provides a quick summary of the results of the experiments in this chapter. Although most of the experiments failed to improve the gravity field solutions based on range-acceleration, it provides a simple visual catalog of what was tried. Here, the grey cell color indicates the default value, the pink cell color signifies no improvement over the default solution, and the green cell color indicates a better performing filter.

CRN, bandwidth (B)	100mHz	80mHz	60mHz	40mHz	20mHz
CRN, convolutions (N_c)	5	7	9	11	13
CRN, span (T_f)	30.7s	50.7s	70.7s	90.7	110.7s
Noise-Robust, span (N)	5	7	9	11	13

Table 4.1: Filter experiments summary

It was discovered that passband reduction in the CRN-filter can actually achieve better results when estimating the Earth's gravity field via range-accelerations. However, as Figure 4.21 shows, even the solution generated with the filter passband at 40mHz, while significantly better in the 120-160 degree range, still fails to compete with the baseline range-rate based solution.

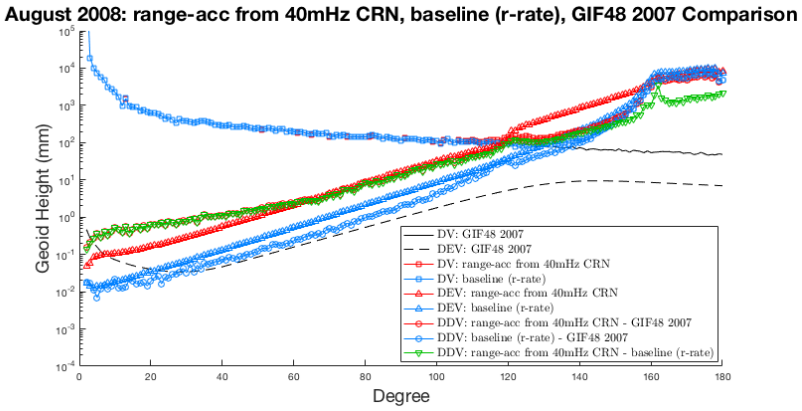

Figure 4.21: 40mHz CRN range-acc vs. baseline range-rate solution

Other choices for computing the derivatives of a noisy signal are plentiful, and include empirical mode decomposition, Savitzky-Golay filtering, the Weiner filter, etc. However, since neither tuning of the CRN-filter, nor the alternate

method, produced even similar solutions to the range-rate generated baseline, the question remains whether the noise induced by differentiation is the only source of corruption in the gravity field. It is possible that all methods of differentiation induce the same or comparable noise in range-acceleration, and that noise is excessive. The current level of technology GRACE possesses onboard may simply produce range measurements noisy enough that they do not allow differentiation with sufficient precision.

Chapter 5

Range-Acceleration Improvements

The previous chapter detailed several attempts to improve upon solutions based on the range-accelerations between the two GRACE satellites. This chapter examines methods that actually achieve the benefits posited from their use in gravity field estimation. This method was suggested by Tregoning [8], and the work of his research group in [7] and [9]. They were able to significantly improve range-acceleration derived solutions, as well as reduce N-S striping errors when working in the mascon domain. This chapter applies the same technique to the realm of spherical harmonics, echoing and substantiating their results, however the conclusions drawn here as to why this method is effective differ from that work.

5.1 Filtering Range Residuals

As in Chapter 2, the GRACE processing algorithm consists of linearizing the system and reducing the quantities involved to residuals by subtracting out a computed reference model. To date, the procedure used for range-rate residuals has not been viable for range-accelerations. There does exist, however, an alternative pathway to arrive at these time derivative signals, which is to instead compute the range residuals first, then time-differentiate that signal twice to obtain range-acceleration residuals. Figure 5.1 diagrams both

the current method of calculation and the proposed alternative technique.

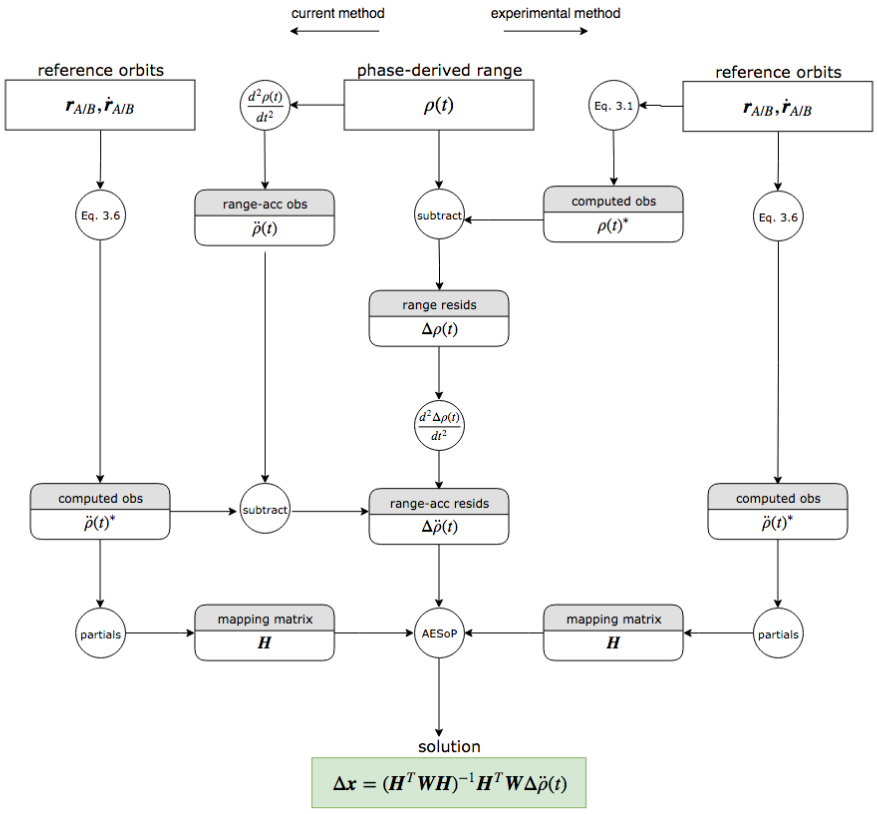

Figure 5.1: Block diagram for both GRACE processing strategies

Both methods seemingly arrive at the same quantity. The next section presents an estimate of the gravity field from a simulation using the second, experimental technique.

5.1.1 2x Differentiation of ρ residuals

Figures 5.2-5.4 display the improved solution provided by first computing the ρ residuals, $\Delta\rho$, then twice differentiating those in time to obtain $\Delta\ddot{\rho}$ as shown in Figure 5.1. It should be noted that even though the initial fit is processing the range measurements, the partial derivatives, which indicate the sensitivities of the measurements to the state parameters, need to be calculated according to the range-acceleration model, as in Equations 3.11 and 3.12. The partials of the range-acceleration w.r.t the position/velocity parameters are computed via these analytical equations (derived in Appendix A), while the partials with respect to the Stokes coefficients and other dynamic parameters have their own Fortran routines for computation in MSODP, detailed by Rim [32].

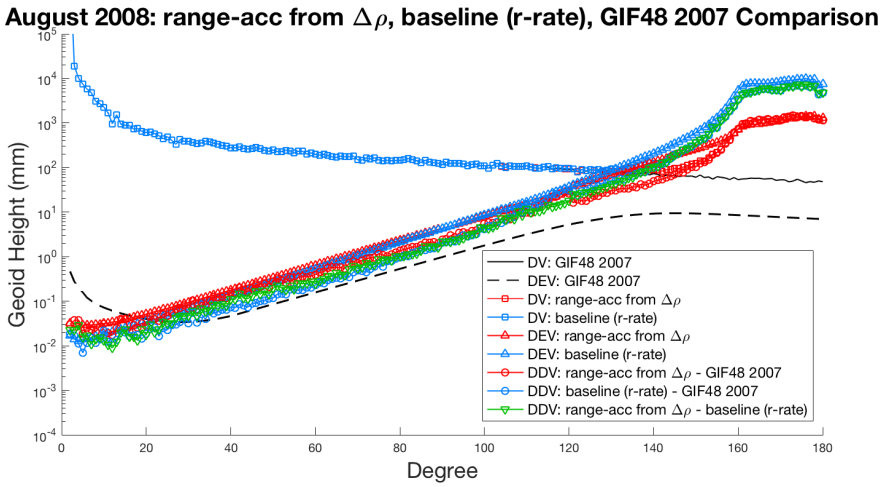

Figure 5.2: DDV/DEV for range-acc solution from 2xdiff $\Delta\rho$

Figure 5.3 maps the anomalies of this estimated gravity field, showing they are reduced in magnitude, much more reminiscent of the baseline range-rate solution than that of the status quo range-accelerations in Figure 3.6. In Figure 5.4, the DDV from the GIF48 truth model is lower at the highest degrees in the range-acceleration solution when compared to the baseline range-rate solution, improving by almost an order of magnitude of by degree-180. The DEV improves similarly. Additionally, the estimates of the Stokes coefficients maintain better fidelity with the truth model up to near degree-140, while the baseline begins to diverge sooner. The DDV triangle plot below nearly avoids having any of the highest magnitude errors on the color scale at all across the entire degree/order spectrum.

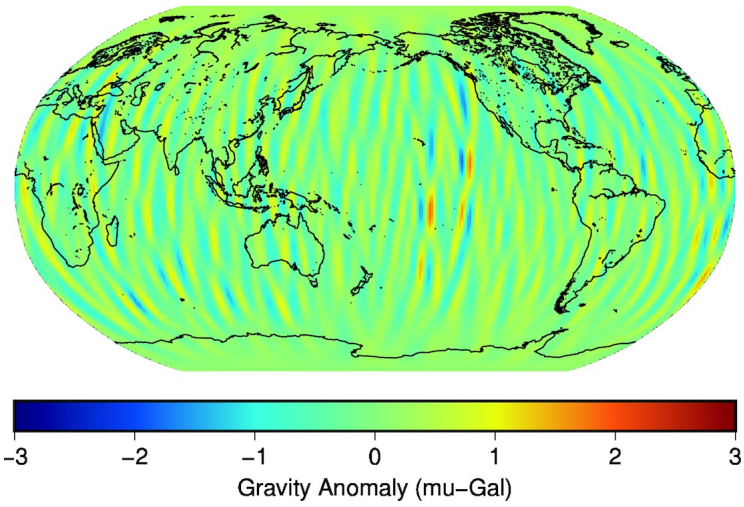

Figure 5.3: Gravity anomaly map for range-acc solution from 2xdiff $\Delta\rho$

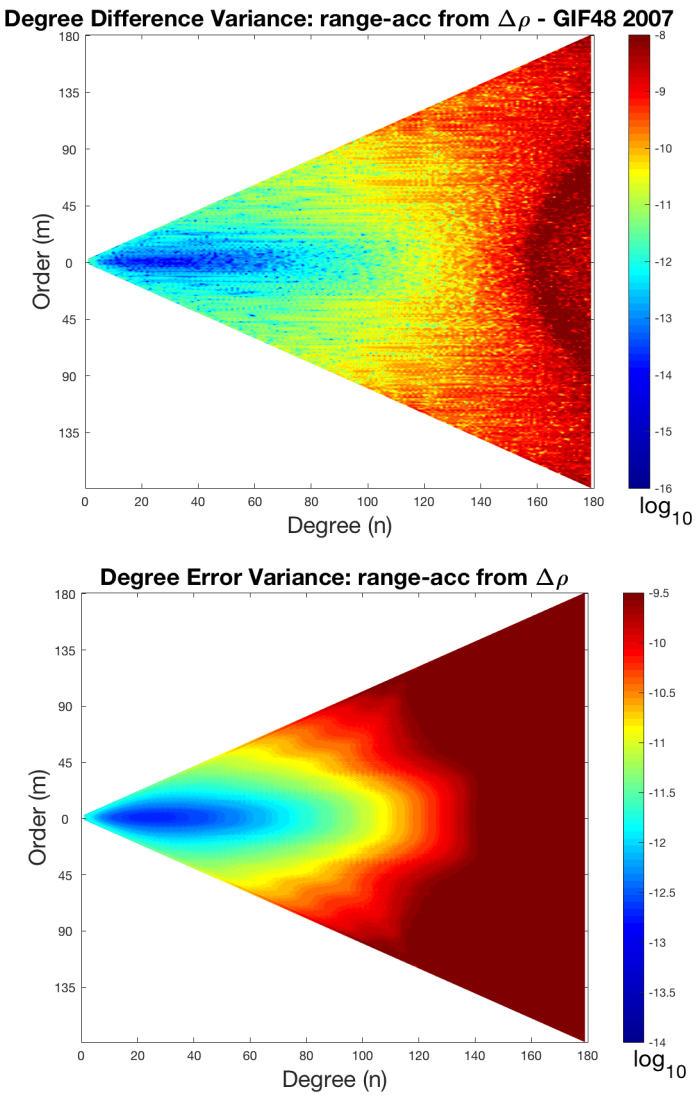

Figure 5.4: DDV/DEV triangle plots for range-acc solution from 2xdiff $\Delta\rho$

5.1.1.1 Method of differentiating the ρ residuals

Both methods of differentiation from this research, the CRN and noise-robust filters, were applied to the range residual process outlined at the outset of the chapter for a comparative analysis. To ensure a like for like comparison, and to remove any unwanted effects possibly introduced by interpolation, a version of the CRN-filter was designed for 5-second input data, as opposed to the higher rate 10Hz data. Figures 5.5 and 5.6 compare the results for the two respective filters when used to differentiate the range residuals. The noise-robust filter was selected for use with this technique because it produces slightly better gravity field results when used in this way.

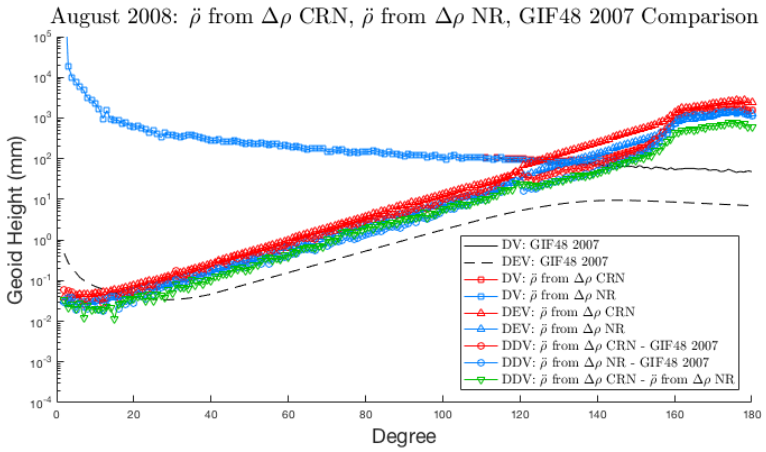

Figure 5.5: DDV/DEV results from applying both filters to the ρ residuals

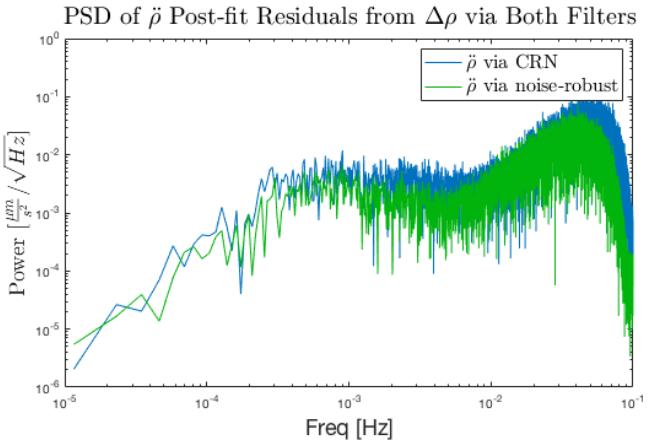

Figure 5.6: PSD of post-fits from applying both filters to the ρ residuals

Both filters show improvement when used on the range residuals instead, however the noise-robust filter just slightly outperforms the CRN-filter. The PSD of the post-fits from the noise-robust filter contains marginally less power than that of the CRN-filter. Similarly, the errors in the solution from the noise-robust filter are lower on the DDV/DEV plot

5.1.1.2 Improvement over standard 40mHz CRN solution

Figure 5.7 displays how differentiating $\Delta\rho$ via the noise-robust filter significantly improves performance over the already improved 40mHz CRN solution by lowering the errors across the entire degree field.

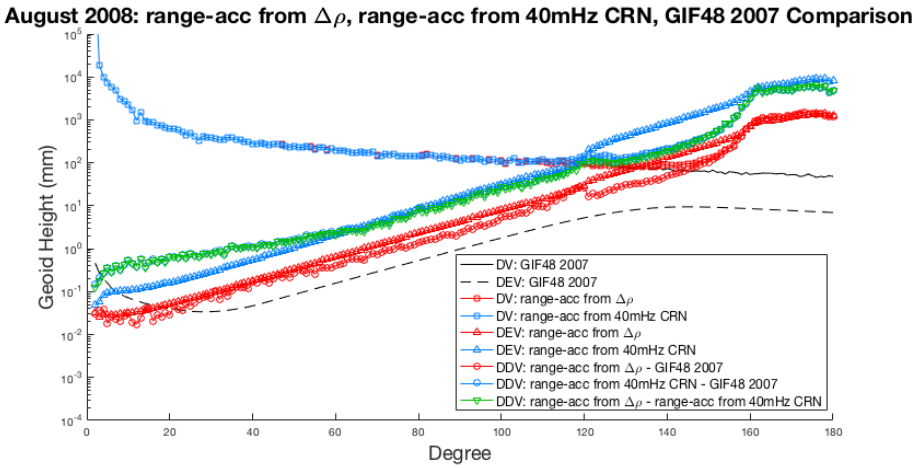

Figure 5.7: Range-acc from $\Delta\rho$ vs. 40mHz CRN case

5.1.2 1x Differentiation of ρ residuals

There is no conceptual reason preventing this method from being applied to the processing of range-rate to see if any benefit may be gleaned from those measurements also. Figure 5.8 compares a solution obtained by differentiating the range-residuals in the time domain only once, then proceeding with the gravity field estimation as usual. Again, it should be noted that the partials are computed with respect to the range-rate observation expression (Equation 3.3), as they are when generating a standard range-rate solution.

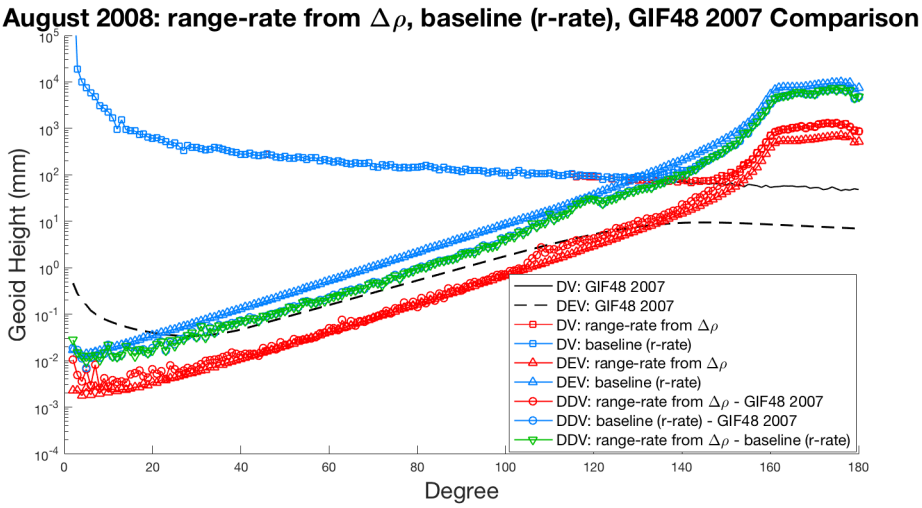

Figure 5.8: DDV/DEV for range-rate solution from 1xdiff $\Delta\rho$

Again, improvement is seen over the baseline solution, with the solution error statistics reducing fairly uniformly across all degrees, $C_{2,0}$ excluded. Processing the range-rate via this new technique benefits the gravity field estimate even more so than applying this method to the range-accelerations. Figure 5.9 compares both the improved range-acceleration and the improved range-rate solution to the GIF48 truth field.

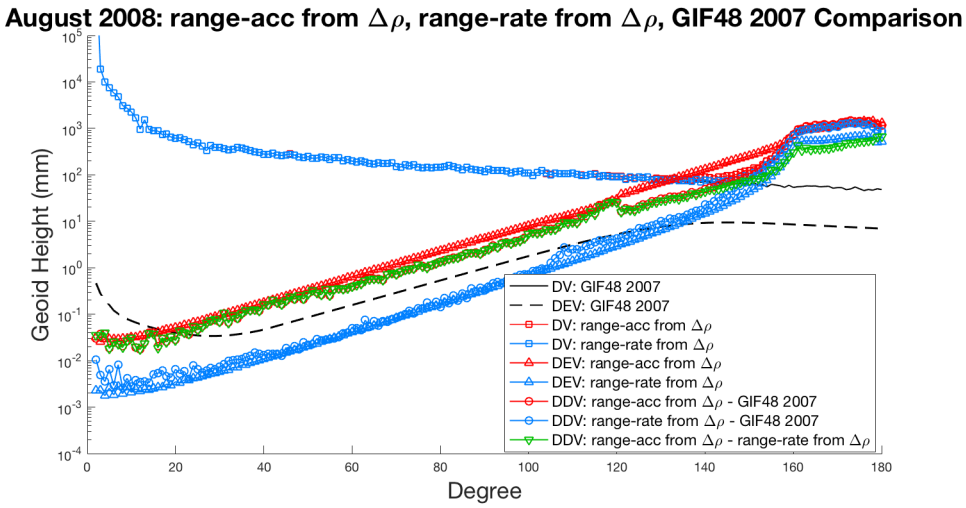

Figure 5.9: DDV/DEV for range-rate and range-acc via new method

5.2 Analysis of Improvement

The rationale for this improvement, as presented by Tregoning, is that the smooth, noise-robust filter does a better job of differentiating the range residuals, resulting in range-acceleration residuals which are much cleaner and better suited for the estimation. This work, however, draws a different conclusion from these results.

The block diagram of Figure 5.1 provides the biggest clue as to why these range-accelerations provide estimates which are an order of magnitude better. While it is true that the same mathematical quantity is arrived at no matter which processing strategy is chosen, the constituent ingredients of

$\Delta\ddot{\rho}$ are vastly different. To obtain the range-acceleration residuals via the improved method, no computation of the range-acceleration model (Equation 3.6) is necessary. This provides an opportunity for improvement, especially considering that the $\ddot{\boldsymbol{r}}_{12}$ inertial acceleration difference vector no longer finds its way into the range-acceleration residuals. Based on these results, it seems that term is a major source of corruption in the gravity field estimates provided by the range-accelerations. While it may seem innocuous, looking back at Equation 2.5 clarifies just how complex the difference in acceleration calculation can be. This computation could be fraught with mismodeling or noisier measurements from other instruments, or both, compounding the issue. At least some portion of the errors in the range-acceleration residuals arise from inherent ACC measurement noise, as well as from errors in rotation/alignment of the ACC data relative to the inertial frame using the SCA data. The new method of generating the range-acceleration residuals, $\Delta\ddot{\rho}$, reduces their contributions by instead relying on computation of the range via Equation 3.1, which is extremely straightforward and includes very little error. By subtracting this calculation from the range observations, then taking the second time derivative of that result, the produced range-acceleration residuals are significantly less noisy, although differentiation does still induce some error at higher frequencies as discussed.

With that stated, the range calculation does still require these noisy quantities, because the necessary precise orbit determination (POD) still needs to integrate the equations of motion, and is still corrupted by ACC+SCA errors in the process of deriving the reference orbit. This fact, however, may actually explain some of the significant noise reduction in the output signals. Contrary to differentiation, which acts as a high-pass filter and increases high-frequency noise, this integration acts as a low-pass filter,. This is effectively smoothing the ACC, SCA, and GPS measurements by a significant amount and suppressing some of their high-frequency error contributions. The status quo method of processing solutions benefits from this integration as well of course, but the benefits are more than offset by adding back in the raw ACC and GPS measurements into the system in order to calculate the observation equations (3.3 and 3.6).

If these claims hold, it would be expected to see signatures in the PSD's of the residuals which agree by showing significantly reduced power in high frequencies, resembling integrated colored noise. Figures 5.10 and 5.11 compare the PSD of the signal for both range-rate and range-acceleration, via both old and new methods, and do exhibit those characteristics.

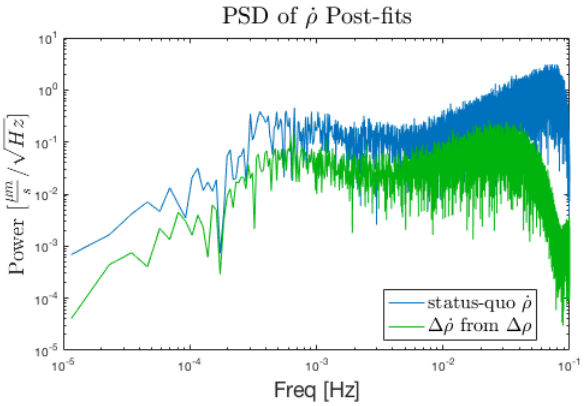

Figure 5.10: PSD comparisons for range-rate with new and old methods

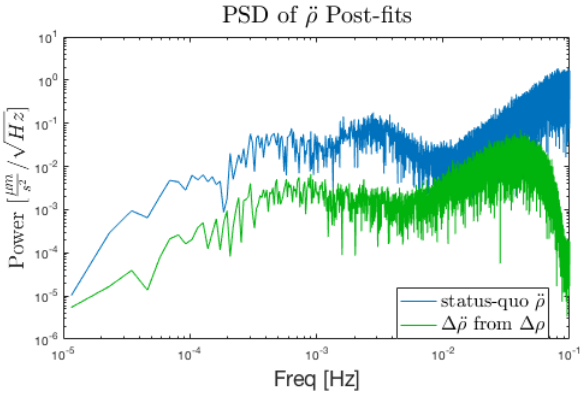

Figure 5.11: PSD comparisons for range-acc with new and old methods

Additionally, as shown in Figures 5.12 and 5.13, this new technique shows results congruent with those produced by removing certain error sources from the system. Figure 5.12 displays how the range-acceleration solution arrived at via this new technique closely resembles, at degree-120 and above, the case in which the ACC noise was set to zero. Similarly, in Figure 5.13, this solution shows similar behavior at low degrees to that of the no GPS error case.

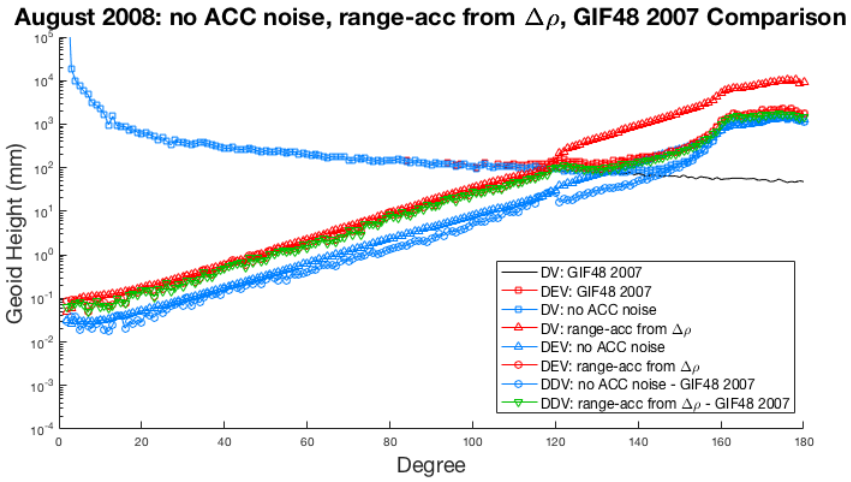

Figure 5.12: Range-acc from $\Delta\rho$ vs. no ACC noise case

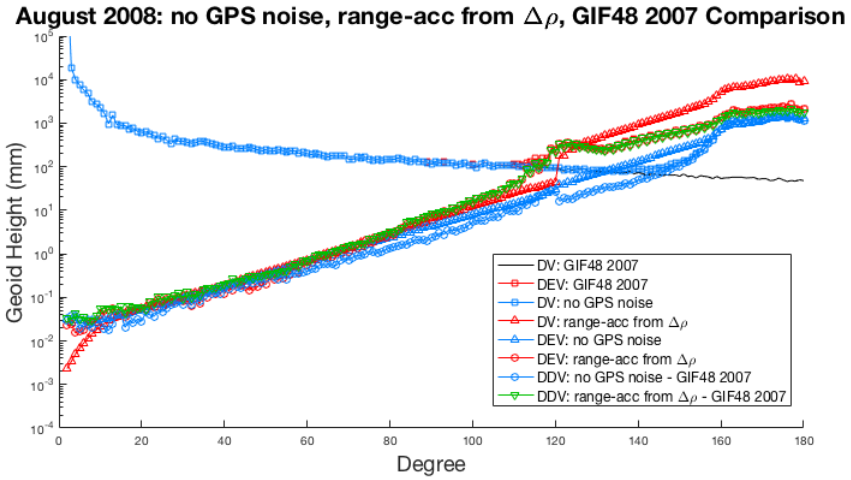

Figure 5.13: Range-acc from $\Delta\rho$ vs. no GPS noise case

Chapter 6

Conclusions

This chapter will provide a brief synopsis of the results of this research, as well as the conclusions drawn from the work. Additionally, this thesis lays groundwork for further study on the topic, and recommendations for future work which may yield benefits in production of official gravity field estimates are provided as well.

6.1 Summary

The range-accelerations are another measurement type available to those processing GRACE mission data, one which potentially contains more spatially localized, higher-frequency information about Earth's gravity field. If true, this would enable more accurate estimation of the spherical harmonic coefficients to higher degree and order than possible with the range-rate observations. At the very least, gravity field estimation with the range-accelerations should yield solutions of similar quality to those with range-rate. To date, however, solutions utilizing the range-accelerations processed similarly via the variational equations have been substantially poorer in quality at best, and are often of no practical use at all. This research set out to understand why this is the case, and to experiment with methods which might mitigate the problems introduced by using the range-accelerations.

First results were as expected, indicating that simply swapping the range-rate observations for range-accelerations and processing as usual cannot produce viable solutions for the Earth's gravity field. The result is riddled with errors and unrealistic estimates of the Stokes coefficients which in no way match reality. The first step taken was to validate that all components of the solution algorithm were indeed correct for the range-accelerations. The outcome showed that both the partial derivatives and simulated noise models are correct, or at least not the primary source of solution degradation.

Current hypotheses suggest that the second time-differentiation of the range signal is the main contributor to these poor solutions, amplifying the noise in the signal at higher degrees, and degrading the SNR to a level which makes accurate recovery of the gravity field impossible. In an effort to test that hypothesis, this research sought to better tune the CRN-filter used for differentiation of the range observations to be more optimal for use with the range-accelerations. Solutions were produced with various filter parameter values, which included adjustments to the passband width, number of self-convolutions, and filter time-span. Most attempts at tuning failed to improve the solutions, usually having little to no effect. It was observed that the selection of passband however, can have a positive influence on the gravity field estimate, moving the errors lower than in the status quo range-acceleration solution. For range-accelerations, the ideal value lies not at the currently

used 100mHz, but somewhere between 40-60mHz, and it is recommended this range be used in the future for solutions which process this measurement type. Still, even with passband tuning, the quality of the range-acceleration based solutions remains inferior to the baseline range-rate solution by a significant margin. As a second attempt at reducing the differentiation-induced noise, a separate differentiator (the"smooth, noise-robust" filter) with properties designed expressly for high-frequency noise suppression was used to produce solutions. This second filter was unable to improve upon the range-acceleration based solutions generated from the default CRN-filter.

The research of another group, led by Tregoning [7],[8],[9], showed promising results with the range-accelerations in the mascon domain, achieving estimates even superior to solutions produced from the range-rate. That work was motivated in a similar way, to reduce the noise introduced into the system by the differentiation of the range. The method they employed was to instead solve for the range-residuals first, and then twice differentiate that input with a noise-robust filter to arrive at the necessary range-acceleration residuals. The same method was employed in the spherical harmonic domain in this research, and remarkable improvement in the range-acceleration based solutions was achieved. Using simulated data, the DDV of the range-acceleration solution produced via this new method were in family with those of the range-rate, resulting in accurate estimation of the truth field up to near degree-140, surpassing that of the range-rate baseline solution. This range-acceleration

solution is comparable to the baseline in DV, DDV and DEV across most of the spectrum, however above degree-140 it achieves better statistics than the baseline, resulting in an estimate closer to the true, reference solution.

6.2 Conclusions

The results produced in this research indicate that the CRN-filter can be better tuned for the GRACE application, at least in the case of range-accelerations, however this tuning is not enough to make these measurements a viable solution processing option. This fact, coupled with the failure of a second filtering method to improve the range-acceleration solutions, points away from the differentiation induced noise being the primary cause of error amplification and poor quality solutions. The technique of filtering the range residuals, as opposed to the range itself, improves the resultant gravity field by such a large degree that other reasons for the increase in accuracy are suggested. In fact, it is noted that this second method bypasses the computation of the range-accelerations with Equation 3.6, which includes the complicated inertial acceleration difference vector. This quantity is fraught with noisy measurements, from the accelerometer for instance, as well as potential mismodeling of multiple geophysical processes, which combine to introduce an amalgamation of errors into the calculation. This new estimation process bypasses the problematic computation, resulting in much less noisy range-acceleration residuals, and solutions generated from them. This new insight, combined

with the higher precision measurements obtained from the GRACE-FO mission, make the range-accelerations promising candidates for use in obtaining cleaner, much more accurate gravity field solutions in the future. It is noted, however, that the calculation of range-acceleration based solutions is far more computationally expensive than those derived from the range-rate, increasing the time needed to obtain a solution by a factor of ∼3-4 for a 180x180 gravity field.

6.3 Recommendations for Future Work

In order to fully test the effectiveness of this new strategy on generating gravity field solutions, the technique would need to be carried out on real mission data as opposed to only simulated observations. This was attempted, but when it comes to real data processing of the range observations there is an ambiguity not as of yet handled robustly in the software. Since the range is derived from the signal phase offsets, there lies an unknown in the processing algorithm, which is the number of full cycles completed by the signal before reaching the other satellite. Due to this uncertainty in the the phase, the range data exhibits discontinuities, or "cycle slips", where the determined number of complete cycles suddenly jumps. This prevents highly accurate calculation of the range residuals, and therefore the second time derivative of that signal would fail to output the same level of precision of range-acceleration residuals as the simulations. A pseudo-test of sorts was run, one in which the range-rate residuals from real mission data were filtered once, and that solution was

compared to a standard range-acceleration solution with real data in Figure 6.1.

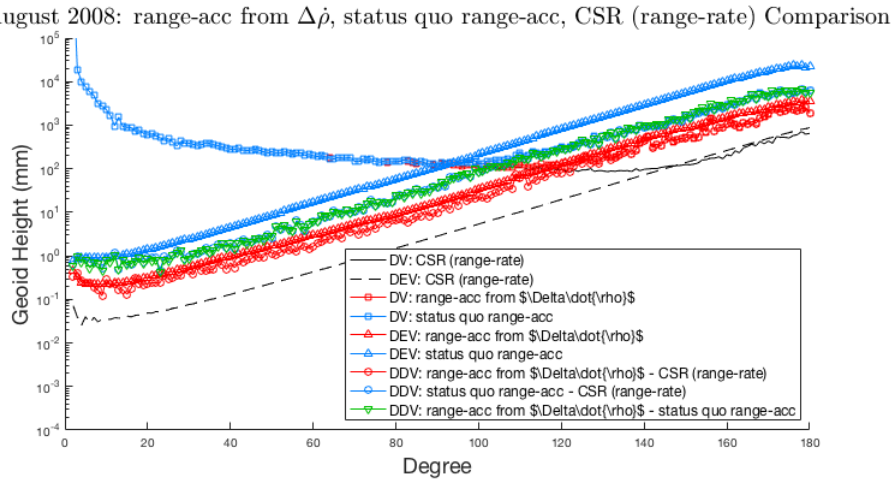

Figure 6.1: Solutions from Real Mission Data

The figure displays at least some promise in implementing the new method for estimating the gravity field with range-accelerations and real flight data. In this comparison, the truth model was the range-rate solution for August 2008 computed by CSR from range-rate observations. While the range-acceleration solution is still well below the quality of the CSR solution, similar improvement to that of Chapter 5 is demonstrated. Under the assumptions of this thesis, the most significant improvements from the new method are given by avoiding computation of Equations 3.3 and 3.6 in the algorithm, so it will be necessary to calculate highly accurate range data, and handle the cycle slips robustly in order to fully test this method for production of actual solutions.

Appendix A

Derivation of Range-Acceleration Partials w.r.t Position and Velocity

This appendix details derivation of the expressions for the partials of range-acceleration w.r.t. the position and velocity of the leading satellite only. The only difference for the trailing satellite are some sign reversals.

$$\ddot{\rho} = \ddot{\boldsymbol{r}}_{12} \cdot \hat{\boldsymbol{e}}_{12} + \frac{1}{\rho}(|\dot{\boldsymbol{r}}_{12}|^2 - \dot{\rho}^2) \tag{A.1}$$

A.1 Position

For simplicity, A.1 has its terms separated and written in terms of $\boldsymbol{r}_{12}$ where possible.

$$\ddot{\rho} = \alpha + \beta + \gamma \tag{A.2}$$

where,

$$\begin{aligned}
\alpha &= \ddot{\boldsymbol{r}}_{12} \cdot \left(\frac{\boldsymbol{r}_{12}}{|\boldsymbol{r}_{12}|}\right), \\
\beta &= \frac{|\dot{\boldsymbol{r}}_{12}|^2}{|\boldsymbol{r}_{12}|}, \\
\gamma &= \frac{(\dot{\boldsymbol{r}}_{12} \cdot \frac{\boldsymbol{r}_{12}}{|\boldsymbol{r}_{12}|})^2}{\boldsymbol{r}_{12}}.
\end{aligned}$$

Some needed terms:

$$\frac{\partial \rho}{\partial \boldsymbol{r}_1} = \frac{\partial |\boldsymbol{r}_{12}|}{\partial \boldsymbol{r}_1} = \frac{\boldsymbol{r}_{12}^T}{|\boldsymbol{r}_{12}|} = \hat{\boldsymbol{e}}_{12}^T$$

$$\frac{\partial \rho^{-1}}{\partial \boldsymbol{r}_1} = \frac{\partial |\boldsymbol{r}_{12}|^{-1}}{\partial \boldsymbol{r}_1} = \frac{-\boldsymbol{r}_{12}^T}{|\boldsymbol{r}_{12}|^3} = \frac{-\boldsymbol{r}_{12}^T}{\rho^3}$$

$$\frac{\partial \boldsymbol{r}_{12}}{\partial \boldsymbol{r}_1} = \boldsymbol{I}$$

$$\frac{\partial \hat{\boldsymbol{e}}_{12}}{\partial \boldsymbol{r}_1} = \frac{\partial (\frac{\boldsymbol{r}_{12}}{|\boldsymbol{r}_{12}|})}{\partial \boldsymbol{r}_1} = \frac{\boldsymbol{I}(\cancel{|\boldsymbol{r}_{12}|}) - \cancel{\boldsymbol{r}_{12}}(\hat{\boldsymbol{e}}_{12}^T)}{|\boldsymbol{r}_{12}|^{\cancel{2}}} = \frac{\boldsymbol{I} - \hat{\boldsymbol{e}_{12}}(\hat{\boldsymbol{e}_{12}}^T)}{\rho}$$

Now the α term,

$$\begin{aligned}\frac{\partial \alpha}{\partial \boldsymbol{r}_1} = \frac{(\ddot{\boldsymbol{r}}_{12} \cdot \hat{\boldsymbol{e}}_{12})}{\partial \boldsymbol{r}_1} &= \frac{\partial \ddot{\boldsymbol{r}}_{12}}{\partial \boldsymbol{r}_1} \cdot \hat{\boldsymbol{e}}_{12} + \frac{\ddot{\boldsymbol{r}}_{12} \cdot (\boldsymbol{I} - \hat{\boldsymbol{e}_{12}}(\hat{\boldsymbol{e}_{12}}^T))}{\rho} \\ &= \frac{\partial \ddot{\boldsymbol{r}}_{12}}{\partial \boldsymbol{r}_1} \cdot \hat{\boldsymbol{e}}_{12} + \frac{\ddot{\boldsymbol{r}}_{12}^T - (\ddot{\boldsymbol{r}}_{12} \cdot \hat{\boldsymbol{e}}_{12})\hat{\boldsymbol{e}_{12}}^T}{\rho}\end{aligned}$$

$$\text{let } \boldsymbol{h} = \ddot{\boldsymbol{r}}_{12} - (\ddot{\boldsymbol{r}}_{12} \cdot \hat{\boldsymbol{e}}_{12})\hat{\boldsymbol{e}_{12}}$$

$$\frac{\partial \alpha}{\partial \boldsymbol{r}_1} = \frac{\partial \ddot{\boldsymbol{r}}_{12}}{\partial \boldsymbol{r}_1} \cdot \hat{\boldsymbol{e}}_{12} + \frac{\boldsymbol{h}^T}{\rho} \tag{A.3}$$

And the β term,

$$\frac{\partial \beta}{\partial \boldsymbol{r}_1} = -\frac{|\dot{\boldsymbol{r}}_{12}|^2 \cdot \boldsymbol{r}_{12}^T}{\rho^3} = \frac{|\dot{\boldsymbol{r}}_{12}|^2 \hat{\boldsymbol{e}}_{12}^T}{\rho^2} \tag{A.4}$$

And the γ term,

$$\frac{\partial \gamma}{\partial \boldsymbol{r}_1} = \frac{-2\dot{\rho}(\dot{\boldsymbol{r}}_{12} \cdot (\boldsymbol{I} - \hat{\boldsymbol{e}}_{12}(\hat{\boldsymbol{e}}_{12}^T)) + \dot{\rho}^2 \hat{\boldsymbol{e}}_{12}}{\rho^2} \tag{A.5}$$

split into two parts,

$$\text{let } \boldsymbol{c}_{12} = \dot{\boldsymbol{r}}_{12} - \dot{\rho}\hat{\boldsymbol{e}}_{12},$$

$$\text{first term } = \frac{-2\dot{\rho}\boldsymbol{c}_{12}^T}{\rho^2} \tag{A.6a}$$

$$\text{second term } = \frac{\dot{\rho}^2\hat{\boldsymbol{e}}_{12}}{\rho^2} \tag{A.6b}$$

combine A.4 and A.6b, and simplify using $|\boldsymbol{c}_{12}|^2$,

$$\text{A.4 + A.6b } = \frac{\dot{\rho}^2\hat{\boldsymbol{e}}_{12}^T - |\dot{\boldsymbol{r}}_{12}|^2\hat{\boldsymbol{e}}_{12}^T}{\rho^2} = \frac{(\dot{\rho}^2 - |\dot{\boldsymbol{r}}_{12}|^2)\hat{\boldsymbol{e}}_{12}^T}{\rho^2},$$

$$|\boldsymbol{c}_{12}|^2 = |\dot{\boldsymbol{r}}_{12}|^2 - \dot{\rho}^2$$

and finally combine A.3, A.4, A.6a, and A.6b into one expression,

$$\frac{\partial\ddot{\rho}}{\partial\boldsymbol{r}_1} = \left[\frac{\partial\ddot{\boldsymbol{r}}_{12}}{\partial\boldsymbol{r}_1}\hat{\boldsymbol{e}}_{12}\right]^T + \frac{1}{\rho}\left[\boldsymbol{h} - \frac{2\dot{\rho}}{\rho}\boldsymbol{c}_{12} - \frac{1}{\rho}|\boldsymbol{c}_{12}|^2\hat{\boldsymbol{e}}_{12}\right]^T \tag{A.7}$$

A.2 Velocity

With these terms already defined, the velocity partial is much more trivial,

$$\begin{aligned}\frac{\partial\ddot{\rho}}{\partial\dot{\boldsymbol{r}}_1} &= \frac{\partial\ddot{\rho}}{\partial\dot{\boldsymbol{r}}_1}\hat{\boldsymbol{e}}_{12} + \frac{\partial}{\partial\dot{\boldsymbol{r}}_1}\left(\frac{|\dot{\boldsymbol{r}}_{12}|^2}{|\boldsymbol{r}_{12}|}\right) - \frac{\partial}{\partial\dot{\boldsymbol{r}}_1}\left(\frac{(\dot{\boldsymbol{r}}_{12}\cdot\hat{\boldsymbol{e}}_{12})^2}{|\boldsymbol{r}_{12}|}\right) \\ &= \frac{\partial\ddot{\rho}}{\partial\dot{\boldsymbol{r}}_1}\hat{\boldsymbol{e}}_{12} + \frac{2\cancel{|\dot{\boldsymbol{r}}_{12}|}\boldsymbol{r}_{12}^{\cdot}}{|\boldsymbol{r}_{12}|\cancel{|\dot{\boldsymbol{r}}_{12}|}} - \frac{2\rho(\boldsymbol{I}\cdot\hat{\boldsymbol{e}}_{12})}{\rho}\end{aligned}$$

$$= \left(\frac{\partial\ddot{\rho}}{\partial\dot{\boldsymbol{r}}_1}\hat{\boldsymbol{e}}_{12}\right)^T + \frac{2\boldsymbol{c}_{12}^T}{\rho} \tag{A.8}$$

Bibliography

[1] Tapley, Byron et al. *The gravity recovery and climate Experiment: Mission overview and early results*. Geophysical Research Letters, 31, 2004

[2] Dunn, Charles, et al. *Instrument of GRACE: GPS augments gravity measurements*. GPS World 14.2 (2003): 16-29.

[3] Touboul, P., et al. *Accelerometers for CHAMP, GRACE and GOCE space missions: synergy and evolution*. Boll. Geof. Teor. Appl 40.3-4 (1999): 321-327.

[4] GRACE Tellus (2018). *GRACE Mission - GRACE Tellus*. `https://grace.jpl.nasa.gov/mission/grace/`.

[5] Kim, Jeongrae. *Simulation study of a low-low satellite-to-satellite tracking mission*. Dissertation, University of Texas at Austin (2000).

[6] Thomas, J. B. *An analysis of gravity-field estimation based on intersatellite dual-1-way biased ranging*. No. JPL-98-15. Jet Propulsion Laboratory, Pasadena, CA, 1999.

[7] Tregoning, Paul. *The role of range acceleration observations in the estimation of sub-monthly temporal gravity fields from GRACE observations* [Abstract]. American Geophysical Union Conference (2017).

[8] Tregoning, Paul. Private Communication.

[9] Tregoning, Paul. *Why Do We Use Range Rate And Not Range Acceleration Observations?* [Presentation]. GRACE Science Team Meeting (2017). Austin, TX.

[10] Wallace, Mark. *A Comparison of Range and Range-Rate Measurements for the Generation of the GRACE Gravity Fields*. Thesis, University of Texas at Austin (2005).

[11] Naeimi, Majid, and Jakob Flury, eds. *Global Gravity Field Modeling from Satellite-to-Satellite Tracking Data*. Springer, 2017.

[12] Tapley, Byron, Schutz, Bob, and Born, George. *Statistical Orbit Determination*. Elsevier, 2004.

[13] Holoborodko, Pavel. *Smooth Noise Robust Differentiators; 2008*. `http://www.holoborodko.com/pavel/numerical-methods/numerical-derivative/smooth-low-noise-differentiators`.

[14] Selesnick, Ivan. *Maximally flat low-pass digital differentiator*. IEEE Transactions on Circuits and Systems II: Analog and Digital Signal Processing 49.3 (2002): 219-223.

[15] McCullough, Christopher Michael. *Gravity field estimation for next generation satellite missions*. Dissertation, University of Texas at Austin (2013).

[16] Bettadpur, Srinivas. *Product specification document*. Center for Space Research, University of Texas at Austin (2007).

[17] Rim, Hyung Jin. *TOPEX orbit determination using GPS tracking system.* (1992).

[18] Gunter, Brian Christopher. *Computational methods and processing strategies for estimating earth's gravity field.* Dissertation, University of Texas at Austin (2004).

[19] Case, Kelley, Gerhard Kruizinga, and Sienchong Wu. *GRACE level 1B data product user handbook.* JPL Publication D-22027 (2002).

[20] Bettadpur, Srinivas. *Level-2 Gravity Field Product User Handbook.* Rev. 4. The GRACE Project. Center for Space Research, Austin, TX (2018).

[21] Bettadpur, S. *UTCSR Level-2 Processing Standards Document for Product Release 06.* The GRACE Project. Center for Space Research, Austin, TX (2018).

[22] Incio, Pedro, et al. *Analysis of star camera errors in GRACE data and their impact on monthly gravity field models.* Journal of Geodesy 89.6 (2015): 551-571.

[23] Kaula, William M. *Inference of variations in the gravity field from satellite-to-satellite range rate.* Journal of Geophysical Research: Solid Earth 88.B10 (1983): 8345-8349.

[24] Kaula, William M. *Theory of Satellite Geodesy.* Dover Publications, Inc. (1966).

[25] Li, Zhao, Tonie van Dam, and Matthias Weigelt. *GRACE gravity field recovery using refined acceleration approach*. EGU General Assembly Conference Abstracts. Vol. 19. 2017.

[26] Goswami, Sujata, et al. *Analysis of GRACE range-rate residuals with focus on KBR instrument system noise*. Advances in Space Research (2018).

[27] Wieczorek, Mark A., and Frederik J. Simons. *Localized spectral analysis on the sphere*. Geophysical Journal International 162.3 (2005): 655-675.

[28] Liu, Xianglin. *Global gravity field recovery from satellite-to-satellite tracking data with the acceleration approach*. (2008).

[29] Cai, Lin, et al. *An analytical method for error analysis of GRACE-like missions based on spectral analysis*. arXiv preprint arXiv:1609.08860 (2016).

[30] Bettapur, Srinivas. Private Communication.

[31] Jet Propulsion Laboratory, Pasadena, CA. Private Communication.

[32] Rim, HJ and Nagel, Peter. *Using MSODP*. Center for Space Research, University of Texas at Austin (2004).